Norwegian University of
Science and Technology

Towards Novel Metal-Polymer Interface Thermal Transport Model Systems

Birger Langebro

Nanotechnology
Submission date: June 2018
Supervisor: Jianying He, KT
Co-supervisor: Susanne Sandell, KT

Norwegian University of Science and Technology
Department of Structural Engineering

Abstract

Enhanced control of thermal transport through metal-polymer interfaces is in demand as metal-polymer composites and organic electronics proliferate while continuous component miniaturization is pursued. Thermal conductivity of polymers is low, therefore thermal boundary conductance (TBC), describing the added resistance of interfaces, only becomes important when polymer component dimensions reach the nanometer scale. TBC is an elusive quantity to measure, requiring advanced experimental setups coupled to system-wide simulations of precisely defined model systems with the mentioned dimensions. Such model systems, for use in three different thermal characterization methods were developed and accurately characterized in this thesis work.

The three targeted characterization techniques 3-omega, frequency domain thermoreflectance, and quasi-static thermal flow, all imposed different constraints on their respective model systems resulting in a total of five different suggested model systems. Three model systems were successfully fabricated, and proofs of concept were given for the remaining two using a combination of spin-coating, dry etching and sputter coating as fabrication methods. In addition, efficient and reliable methods for characterizing thickness, thickness uniformity, sub-nanometer surface roughness, bulk structure and polymer orientation using white light interferometry, µ-Raman spectroscopy, atomic force microscopy (AFM), scanning electron microscopy (SEM) and scotch-tape adhesion testing were developed, and results were verified to be in accordance with published literature. Noticeably, a gentle and rapid method for smooth step edge fabrication was developed, metal interface structures of a metal film peeled from a polymer substrate were mapped using AFM, and a free-standing poly-methyl methacrylate (PMMA) thin film was achieved through release from a poly(vinyl alcohol) (PVA) layer in water.

From completed model systems it was learned that sputtered Au adhered poorly to both as-received and spincoated PMMA. On the other hand, spincoated polymer adhered strongly to all substrates, indicating large interface differences, which were

confirmed by AFM characterization of interfacial voids in the sputtered Au film. The bulk composition of metal films was found to consist of columnar grains, based on AFM nanomechanical mapping of metal surfaces for a range of different film thicknesses. Polymer bulk composition was found to not be affected by the spincoating process.

Important steps have been made in fabricating and understanding these metal-polymer model systems, but work on accurate interface characterization still remains. It must also be verified that the chosen geometries can yield accurate TBC values in thermal conductivity measurements.

Sammendrag

I forbindelse med utviklingen av komposittmaterialer av metall og polymer, samt fleksibel elektronikk, kreves bedre kontroll av varmetransport gjennom grenseflaten mellom metall og polymer. Ettersom polymerer har eksepsjonelt begrenset varmeledning blir effekten av dårlig grensevarmeledning bare viktig når materialene er på størrelse med noen få nanometer. For å forstå grensevarmeledning bedre kreves avanserte eksperimenter og simuleringer av nøye definerte modellsystemer. Slike modellsystemer for tre forskjellige eksperimentelle metoder ble utviklet og nøye karakterisert i denne masteroppgaven

De tre metodene for å måle grensevarmeledning, nemlig termorefleektans i frekvens-domenet, 3-omega og kvasistatisk varmeledning, hadde alle forskjellige krav til modellsystemene som kunne brukes. Av totalt fem planlagte modellsystemer ble tre realisert og to ble delvis realisert, alt ved en kombinasjon av rotasjonsbelegging, tørr-etsing og sputtring. I tillegg har pålitelige og effektive metoder for å karakterisere filmtykkelse, overflateruhet, bulkstruktur og polymerorientering ved bruk av interferensmikroskopi, µ-Raman-spektroskopi, atomkraftmikroskopi (AFM), sveipeelektronmikroskopi og teip-testing blitt utviklet og resultatene fra disse har blitt sammenliknet med resultater fra litteraturen. Verdt å merke seg er utviklingen av en mild og rask måte for å lage trinn i PMMA-filmer, avbilding av metallsiden av en metall-polymer grense ved bruk av atomkraftmikroskopi og fabrikering av en frittstående poly(metyl metakrylat) (PMMA)-film ved hjelp av vannløselig poly(vinyl alkohol) (PVA).

De produserte modellsystemene ble analysert i detalj. Sputtret gull hadde vesentlig dårligere adhesjon til PMMA-substrater enn PMMA rotasjonsbelagt på gullsubstrater. AFM-undersøkelser viste at dette skyldtes hulrom i grenseflaten til gullaget. Fra overflateskruturen til metallfilmene var det tydelig at de bestod av kolonneformede korn pakket i amorft materiale. µ-Raman-spektroskopi viste at PMMA-filmene ikke var strukturelt forskjellig fra PMMA i bulk.

Dette arbeidet har ført til økt forståelsen av disse metall-polymer-modell-systemene, men karakterisering av grenseflaten gjenstår fortsatt. Det gjenstår også å teste at modellsystemene faktisk gir grensevarmeledningsmålinger med ønsket møyatkighet.

Preface

My supervisor Jianying He is acknowledged for invaluable discussions, guidance and feedback during the course of the project and thesis work. My co-supervisor Susanne Sandell is acknowledged for filling me in on details about characterization techniques and for finding suitable sample dimensions. Helge Kristiansen and Jianying He had the initial idea about the double-sided metal coated polymer for use in quasi-static thermal flow characterization. The lab technicians and other staff at NanoLab are acknowledges for all instrument training and help in running a highly functional clean room facility. Especially Einar Digernes is acnowledged for performing carbon evaporation coating at very short notice. Ruth G. Li is acknowledged for supplying PDMS slabs for peel testing, for proof-reading this thesis and for being an awesome study and life companion for the past four and a half years. The Research Council of Norway is acknowledged for the support to the Norwegian Micro- and Nano-Fabrication Facility, NorFab, project number 245963/F50. The Research Council of Norway is also acknowledged for the support to the Engineering Metal-Polymer Interface for Enhanced Heat Transfer project, project number 251068. This thesis work is a continuation of a project work titled *Synthesis and multiphysical characterization of metal-polymer thin films* from 2017, thus portions of the theory are identical to that of [1].

Contents

Abstract • i

Preface • v

Abbreviations • ix

1 Introduction • 1

2 Theory • 5

2.1 Metal-polymer thermal boundary conductance (engineering perspective) • 5
2.2 Characterization of thin film thermal transport • 7
2.3 Model system and material properties summary • 11
2.4 Fabrication methods • 14
2.5 Characterization methods • 21

3 Materials & Methods • 29

3.1 Materials • 29
3.2 Spincoating PMMA on test substrates • 30
3.3 Problems of film thickness measurements • 31
3.4 Surface morphology measurements • 34
3.5 Fabrication of 3-omega samples • 36
3.6 Fabrication of FDTR I samples • 38
3.7 Fabrication of FDTR II samples • 38
3.8 Fabrication of FDTR III and QSTF model systems with concurrent adhesion testing • 39

3.9 Water soluble release layer • 42
3.10 μ-Raman spectroscopy • 43
3.11 Adhesion testing • 43
3.12 Field-effect scanning electron microscopy • 43

4 Results • 45

4.1 Towards spincoating thickness • 45
4.2 Polymer film thickness for FDTR II and 3ω model systems • 47
4.3 Surface and interface roughness • 50
4.4 Defects quantification • 51
4.5 Polymer bulk structure by μ-Raman spectroscopy • 54
4.6 Polymer molecular chain alignment • 56
4.7 Metal growth • 57
4.8 Novel water soluble release layer for QSTF model fabrication • 61

5 Discussion • 63

5.1 Step height fabrication • 63
5.2 Thickness measurement • 63
5.3 Spincoating of polymer films • 65
5.4 Sample roughness and defect quantification • 65
5.5 μ-Raman spectroscopy of PMMA • 68
5.6 Metal structure • 69
5.7 Carbon coating • 71
5.8 PVA release layer and QSTF model systems • 71
5.9 Metal-polymer interface properties • 72

6 Conclusion • 75

Further work • 77

Bibliography • 80

Postscript • 89

Abbreviations

AC	Alternating current
AFM	Atomic force microscope/microscopy
BSE	Backscattered electrons
CCD	Charge-coupled device
DC	Direct current
FDTR	Frequency domain thermoreflectance
FE-SEM	Field effect scanning electron microscope/microscopy
ICA	Isotropic conductive adhesive
IPA	Isopropyl alcohol
PF-QNM	PeakForce quantitative nanomechanical mapping
PMMA	Poly(mehtyl methacrylate)
PS	Poly(styrene)
PVA	Poly(vinyl alcohol)
PSI	Phase scanning interferometry
QCM	Quartz crystal microbalance
QSTF	Quasi-static thermal flow
SZM	Structural zone model
TBC	Thermal boundary conductance
VSI	Vertical scanning interferometry
VXI	Software enhanced vertical scanning interferometry
XRR	X-ray reflectometry
XPS	X-ray photoelectron spectroscopy

1 Introduction

Continued technological advancement in diverse fields such as microelectronics, bulk composites and organic electronics are placing heavy strain on current heat management technology and fundamental understanding of thermal transport especially at the nanoscale [2]. In microelectronics, nanoscale feature sizes yield higher heat generation per volume, which becomes a problem as the intrinsic large amount of interfaces acts as barriers to thermal transport [3, 4]. Generated heat also needs to be removed from devices on macro-scale where easily processable composite glues can be applied [3], often comprising filler particles with interfaces that again impede thermal transport [5, 6]. Organic electronics such as organic light emitting diodes, organic solar cells and flexible electronics all rely on a high amount of interfaces between the active, insulating or semiconducting polymer and conductive metal wiring [7, 8]. In all these applications heat has to pass through interfaces with a finite conductance called the thermal boundary conductance (TBC), different from, and generally lower than that of the bulk. This nanoscale thermal transport feature only becomes of importance when dimensions in the material approaches the Kapitza length, close to the phonon mean free path [2, 4]. There also exists applications where low TBC is targeted to minimize overall thermal conductivity such as in thermoelectric materials [5, 9].

Compared to the massive steps taken in understanding of photons and electrons in the last decades, advances in theoretical and technological understanding of phonons have been very limited [10]; Partly due to the low energy and rapid timeframes associated with phonons, rendering measurement hard, and partly due to the lack of

need as the problems mentioned above only arose from highly demanding applications of photons and electrons [4]. The concept of phonons as atomic vibrations exhibiting wave-particle duality is being questioned as it seems to only yield acceptable predictions for highly idealized crystal structures [11]. Indeed, for amorphous materials, the situation becomes more severe and theoretical predictions deviating from experimental observations by up to 40 % are considered acceptable [7, 12]. Thus the theoretical foundation for understanding TBC is missing a complete understanding of vibrational transport on either side of the interface, which for the case of polymers is further complicated by the complex geometry and low bulk conductivity complicating both modeling and experimental studies [7, 12].

Metal-polymer interfaces are technologically and theoretically interesting, however, understanding and controlled manipulation of TBC are lacking. Only recently the important effect of chemical bonds at the interface, was measured and quantified [8, 13]. Other effects remain open for proper characterization, with coupling between metal electrons and phonons vibrational states being totally unexplored. Suggestions for improving TBC in the metal-dielectric interface are generally focused on improving phonon transport with for example adhesion layers [14], phonon focusing nanostructures [15] or mass-graded interfaces [16].

At the Norwegian University for Science and Technology, the Nanomechanics group, spearheaded by professor Jianying He is moving into this exciting area with the goal of developing a new class of thermal interface materials for improving TBC in applications with extremely high amounts of metal-polymer surface area. From a study of silver coated polymer micro spheres for use as isotropic conductive adhesives (ICAs), it was discovered that the high amount of polymer metal contacts significantly impeded heat transport through the ICA despite high electrical conductivity [17]. The Engineering Metal-Polymer Interfaces for Enhanced Heat Transfer (HEFACE) project, funded by the Norwegian Research Council was initiated to study metal polymer interface properties through both experiment and simulation to gain additional insights into this complicated and interesting system. Further, it is desirable to develop thermal interface materials for improving thermal transport between dissimilar materials and apply these to the earlier mentioned silver coated micro spheres to improve thermal conductivity of the ICA.

Comparing measured results to computer simulations require exceptional knowledge of structure, composition and chemistry of both interface and bulk materials used in model systems. The three thermal characterization methods 3-omega (3ω), frequency domain thermoreflectance (FDTR) and quasi-static thermal flow (QSTF)

will act to independently verify obtained results as TBC is an exceptionally difficult quantity to measure for thermally insulating materials [4, 18]. These characterization methods all require different variations of laminar polymer metal structures with metal and polymer layers varying in thickness and stacking order. Furthermore, strategies for controlling TBC are to be investigated, so the model systems should be compatible with the addition of interface materials or nanostructures. As interface and material microstructure is determined by sample fabrication, the development of tools for characterizing these properties of each model system is essential. Both 3ω and QSTF requires samples of multiple polymer thicknesses, thus rapid fabrication and characterization is desirable to be able to iterate through a larger number of model systems and interface modifications in less time.

In this master thesis work, five different model systems are pursued with the goals of rapid repeatable fabrication and complete knowledge of bulk, interface and surface properties. Features of interest include polymer and metal bulk structure, as well as roughness, morphology and chemical composition of the interface of each model system, as summarized in Figures 2.4 and 2.5. Fabrication of polymer thin films will, based on a previous literature study [1], be limited to spincoating of poly(methyl methacrylate) (PMMA). Fabrication of metal thin films will be limited to e-beam evaporation and magnetron DC sputter coating of predominantly Au and Cu. Characterization tools are chosen based on availability, speed of data acquisition and precision for each material and size range. Several new methods are developed, including batch step edge fabrication, a water soluble release layer, automated defect quantification and inspection of both sides of sputter deposited thin metal films. In addition, one model system for 3ω and two model systems for FDTR are successfully developed, while feasibility is proven for one melt-processes FDTR model and a QSTF model.

Each chapter is structured according to the natural progress of the work with characterization tools used during fabrication, preliminary optimization, actual fabrication results and characterization of produced model systems. Where applicable, such as in the case of failed methods, fundamental investigations, or rapid iterations, methods, results and discussion may be mixed in one section. As different model systems of varying geometry are pursued, the reader is referred to Figures 2.4 to 2.6 for a systematic overview of model systems and properties to be studied. A postscript with experimental findings and fabrication results not available during the writing of this thesis can be found after the bibliography.

2
Theory

This chapter first elaborates on TBC between metal and polymer before going into the three different thermal characterization methods for which samples are to be fabricated. An overview of relevant material and interface properties as well as an overview of model systems and fabrication pathways is given in the form of figures. Subsequently theory on important aspects of the chosen fabrication methods is given with a detailed review of metal thin film growth both on the substrate and in the film bulk. Theory of the various characterization methods is given last.

2.1 Metal-polymer thermal boundary conductance (engineering perspective)

In nanoscale systems or systems with a high density of interfaces between dissimilar materials, transport of heat occurs by other pathways than in bulk materials and is called nanoscale thermal transport. For systems consisting of insulators and metals, such as those that will be discussed in this thesis, a complete understanding of phonon-phonon and phonon-electron interactions is essential to understand TBC. Furthermore, interface chemistry, physics and morphology, such as the presence of interface layers and nanostructuring is highly significant. Together, these factors make up a series of resistances to the heat flow across an interface. [5, 6, 13]

A temperature difference (ΔT) across an interface of a given area (A) with boundary conductance (G) results in a flow of energy (P) according to $P = GA\Delta T$.

Commonly, G has the unit W/m^{2}K [2]. Bulk conductivity (k) of a material of a certain length (L) is similarly found as $k = \frac{PL}{A\Delta T}$. A refers to the apparent contact area as the true contact area, which also takes interfacial roughness and voids into account, is generally not known. G and k can be further broken down into contribution from electrons (G_{el} and k_{el}) and phonons (G_{ph} and k_{ph}). For conductive materials, electrons dominate heat transport, where hot free electrons transfer kinetic energy through Coulomb interactions. Electronic heat conduction through an interface is facilitated by low amount of defects and the two materials having a closely matching heat capacity and Fermi velocity [19].

Lattice or molecular vibrations (i.e. phonons) are the main heat carriers for all other ordered and amorphous materials. Phonons have wave-particle duality like photons, including properties such as polarization, direction and frequency. To allow efficient phonon transmission through an interface, the two materials should have closely matching vibrational properties and the interface area should be large, defect free and have strong chemical and mechanical bonds. Any deviation from these rules will cause unwanted phonon scattering. [2]

The interaction of electrons and phonons in a metal is commonly modeled as a two temperature system with an electron (T_{el}) and a phonon temperature (T_{ph}). Transfer of heat from one carrier to the other is governed by the electron-phonon coupling parameter ($g(T)$). For metal layers of thickness L thinner than the characteristic length scale of equilibration ($\sqrt{\frac{k_{ph}}{g}} \approx 100\,\mathrm{nm}$), contribution to interface conduction from g can be modeled as a conductor ($Lg(T)$) in series with electronic boundary conductance (G_{el}) and in parallel with phononic boundary conductance (G_{ph}) [20]. By summation, the total interface thermal conductance becomes

$$G_{tot} = \left(\frac{1}{G_{el}} + \frac{1}{Lg(T)} \right)^{-1} + G_{ph} \tag{2.1}$$

No discussion of temperature equlibration in the case of $T_{ph} > T_{el}$, have been found in literature. Studies of composite materials with carbon nanotube (CNT) and graphene fillers have, in addition to low boundary conductance revealed an added heat resistance of the fillers due to internal phonon scattering. Low frequency phonons from the surrounding polymer matrix enters the CNT, in which they are scattered to more favorable high frequency phonons, before again having to go back to a low frequency state to transfer to the matrix. k_{ph} of the CNT filler is therefore much lower than the values measured or calculated for freestanding CNTs. Thus, thermal energy transfer in a composite is hampered both by interfaces and materials

exhibiting lower thermal conductivity compared to their bulk form. [2]

2.2 Characterization of thin film thermal transport

3-omega method

The 3ω method was introduced by Cahill and Pohl in 1987 as a development of the hot wire and hot strip techniques for the measurement of material thermal conductivity [21]. The method is based on a single metal wire acting both as heater and thermometer through joule-heating and temperature dependent resistance, respectively. A rectangular µm wide metal wire with connection pads is deposited onto the material to be measured as seen in Figure 2.1a and b, and connected to electrical measurement equipment. A modulated alternating current (AC) signal is passed through the wire, causing a double frequency (2ω) heating of the wire with amplitude and phase determined by the thermal conductivity of the underlying material. The heating of the wire induces a varying resistance ($R(2\omega)$), which, multiplied by the original current ($I(\omega)$) can be measured as a third harmonic voltage oscillation ($V(3\omega)$) using a lock-in amplifier. The measured voltage harmonics 3ω and 1ω are related to the amplitude of temperature oscillations (ΔT) by

$$\Delta T_{2\omega} = \frac{2}{\alpha} \frac{V_{3\omega,RMS}}{V_{1\omega,RMS}},$$

where α is the temperature coefficient of thermal resistivity of the metal wire.

To measure thermal boundary conductance (G) between a film and a substrate, a

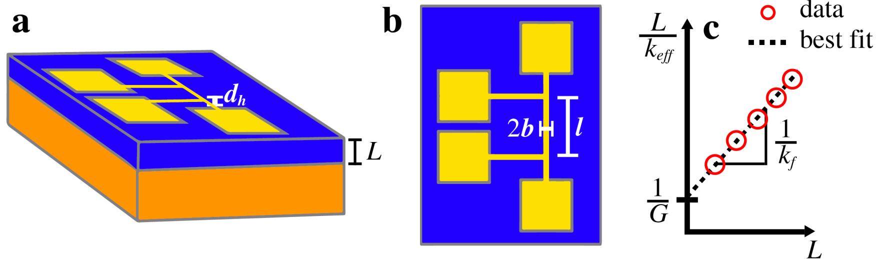

Figure 2.1. Illustration of 3ω measurement of thin films (**a**) and generalized wiring geometries (**b**). **c**, fitting of data measured by differential 3ω , where thermal boundary conductance can be extracted directly.

series of samples with thin films of different thicknesses (L) deposited between metal wire and substrate should be characterized. In the case of heater width ($2b$) much larger than L, heat flow in the in-plane direction $k_{f\|}$ can be disregarded and the film effective conductivity (k_{eff}) simply results in a frequency-independent temperature drop (ΔT_f) adding to that of the substrate (ΔT_s) as ($\Delta T_{tot} = \Delta T_s + \Delta T_f$). The temperature drop of the film is obtained from Fourier's law as

$$\Delta T_f = \int_0^L \frac{q_l}{2bk_{eff}} dy = \frac{P_l L}{2b(k_{eff})},$$

where q_l is the power dissipated from the wire per unit area. Rearranging yields

$$k_{eff} = \frac{P_l L}{2b(T_{tot} - T_s)}. \tag{2.2}$$

(2.2) is used for simple 3ω setups. More commonly, differential measurements are performed to isolate film effects from those of the substrate and measurement system. In differential 3ω , $\frac{L}{k_{eff}}$ is a series resistance of the film thermal resistance ($\frac{L}{k_f}$) and $\frac{1}{G}$ as

$$\frac{L}{k_{eff}} = \left[\frac{L}{k_f} + \frac{1}{G}\right]^{-1}. \tag{2.3}$$

By plotting $\frac{L}{k_{eff}}$ as a function of L, G can be found from the y-intercept of (2.3) as illustrated in Figure 2.1c. [22, p. 45-58]

Assumptions relevant for the above deductions put restrictions on film thickness with respect to thermal penetration depth of the film (λ_f) and metal wire thickness (d_h). The penetration depth is found from thermal diffusivity (D) and signal frequency (ω) as

$$\lambda_f = \sqrt{\frac{D}{2\omega}}. \tag{2.4}$$

With the constraints $L < 5\lambda_f$ and $L \gg d_h$, it is readily seen that the film must satisfy $100\,\mathrm{nm} \ll L < 4.6\,\mu\mathrm{m}$ for a film of $D = 1.2 \times 10^{-7}$, a frequency range of 10-110 000 Hz and a conductor of $d_h = 100\,\mathrm{nm}$ [22, p. 58-60]. These values were chosen based on the experimental setup and PMMA thin films to be studied in this thesis. Other constraints are placed on the system geometries by the penetration depth, ultimately determining the accuracy of measured values.

Frequency-domain thermoreflectance method

FDTR utilizes temperature-dependent surface reflectivity (i.e. thermoreflectivity) to measure different heat diffusion mechanisms of thin film systems. In a setup based on two continuous wave lasers, seen Figure 2.2a, the pump laser heats a sample with varying light modulation frequency (ω_0) and the probe laser measures the sample response to heating. Reflectance change of the reflective transducer layer upon heating is manifested in the probe-beam as a frequency dependent amplitude and phase shift ($Z(\omega_0)$). Theoretical material response is calculated by considering a Gaussian intensity distribution of the pump beam, solving the Fourier heat equation for the material stack, and weighting the resulting surface temperature on the Gaussian intensity distribution of the probe beam. By performing a non-linear least square fit on the measured phase shift as a function of modulation frequency illustrated in Figure 2.2b, system parameters such as in-plane ($k_{\|}$) and cross-plane ($k_{\perp}$) thermal conductivity, TBC (G), and volumetric heat capacity (C) can be extracted. However, more than two parameters can only be determined simultaneously in the case of materials of thermal diffusivity higher than 3×10^{-6} m^2/s [23]. As roughness is a major contributor to non-specular scattering, transducer roughness should be lower than 15 nm to get sufficient signal [2]. For an in-depth theoretical introduction, the reader is referenced to [23] for experimental setup and [24] for theoretical considerations.

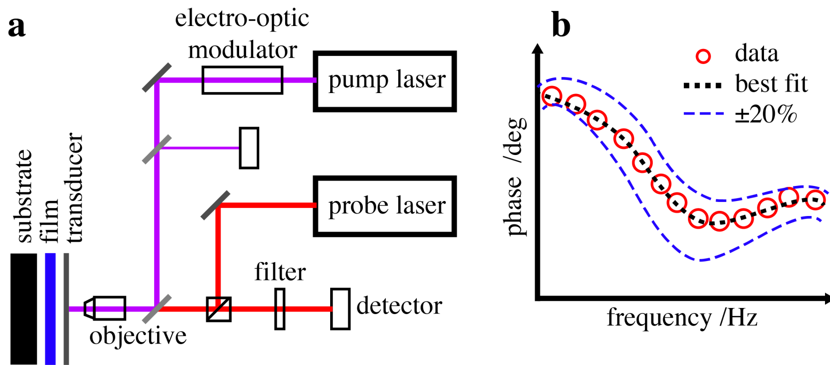

Figure 2.2. Illustration of frequency domain thermoreflectance setup (**a**) and fitting to the resultant data (**b**).

Quasi-static thermal flow method

QSTF is based on the common absolute thermal flow measurement where a series of thermocouples are placed in succession on both sides of a material interface as illustrated in Figure 2.3. When heating one side and cooling the other, the heat impedance of the interface can be calculated from the heat flux (q) and change in temperature over the interface (ΔT). q is found from the change along the bars as

$$q = \left(\frac{dT_1}{dx} + \frac{dT_2}{dx} \right) /2.$$

By introducing new materials of a controlled thickness (L) in the interface, ΔT changes according to the properties of the new materials from which effective thermal conductivity (k_{eff}) can be found from

$$\Delta T(L) = \frac{qL}{k_{eff}}. \tag{2.5}$$

Linearization followed by plotting is performed as for 3ω , however, as there are now multiple layers in the material interface, the thermal resistance of the y-intercept must include all remaining n layers and m interfaces:

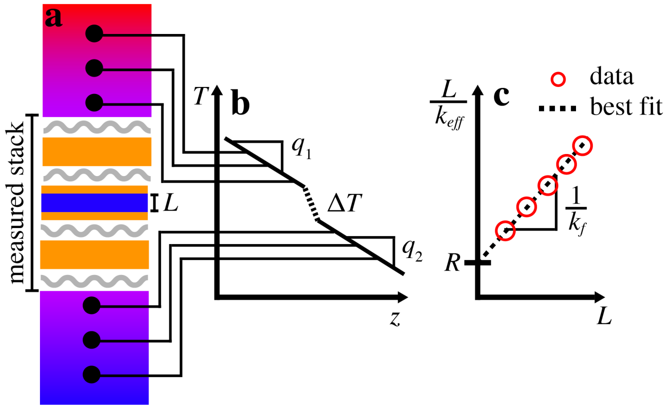

Figure 2.3. a, illustration of quasi-static thermal flow setup with labeled sample stack placed in the interface. **b**, fitting of the measured data to extract film conductivity and remaining thermal resistance from which thermal boundary conductance can be extracted.

$$R = \sum_n \frac{L_n}{k_n} + \sum_m \frac{1}{G_m} \tag{2.6}$$

If all L_n, k_n and G_n are known or are very small, G_f of the two film boundaries can be extracted from the last sum and solved as

$$G_f = 2\left[R - \sum_n \frac{L_n}{k_n} - \sum_{m-2} \frac{1}{G_m}\right]^{-1}. \tag{2.7}$$

As L_n, k_n and G_n are most likely not known, the remaining thermal resistance (R_0) can be measured prior to introducing the film, reducing (2.7) to

$$G_f = 2(R - R_0)^{-1}. \tag{2.8}$$

2.3 Model system and material properties summary

Illustrations of material and interface properties are given in Figures 2.4 and 2.5, respectively. The term bulk is used to separate interior properties of thin films to properties of the near interface regions. All bulk properties will be investigated and results analyzed based on available literature. Of the mentioned interface properties, roughness and presence of voids will be probed directly, while adhesion is used to probe the combined effects of all interface properties. Model systems summarized in Figure 2.6 are prepared by different methods and in different stacking order as governed by their target thermal characterization method. FDTR requires a transducer with low roughness and high coefficient of thermoreflectivity, deposited on top of either a bulk (a and c) or thin film (b) polymer depending on the model used to interpret FDTR data. 3ω data analysis ignores TBC between metal heater and polymer, thus the measured TBC is that between the polymer thin film and the substrate. Au covered Si substrates coated with five different PMMA thicknesses to permit extrapolation to zero thickness, should therefore be suitable model systems for the 3ω method. 3ω wiring deposition will not be performed as a part of this thesis work as this equipment was located abroad. QSTF requires polymer films of five different thicknesses to be placed between two highly conductive metal blocks. However, commercially supplied metal pieces and rolled films tends to have surface roughness much higher than the $<$100 nm thickness of the intended polymer films. As an alternative, metal deposition could therefore be used to coat both sides of a

polymer film before attaching the metal-polymer sandwich to the metal blocks with gap-filling high conductivity thermal paste. Like the 3ω method, QSTF also requires films of five different thicknesses, placing some constraint on the time needed to produce samples of each film thickness. Fabrication flowcharts of Figure 2.6 are simplified, and full descriptions can be found in Chapter 3.

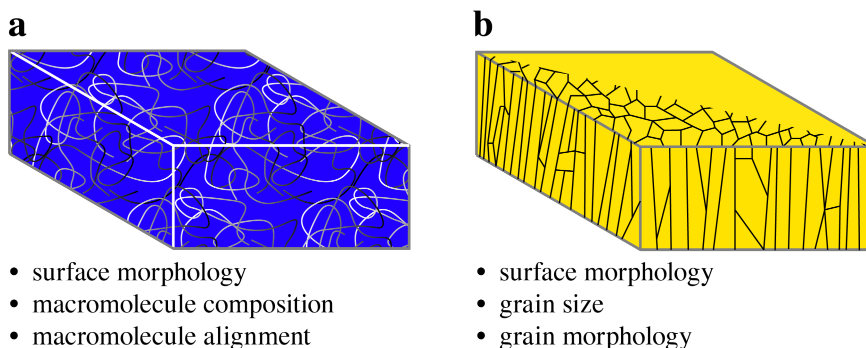

Figure 2.4. Overview of relevant material properties discussed in this thesis. **a**, amorphous insulating polymer. **b**, metal thin film.

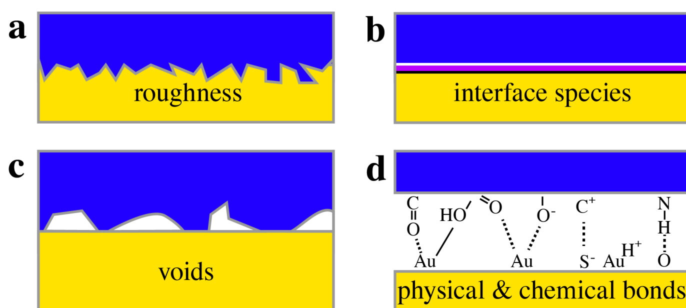

Figure 2.5. Overview of relevant interface properties between metal (yellow) and polymer (blue) discussed in this thesis.

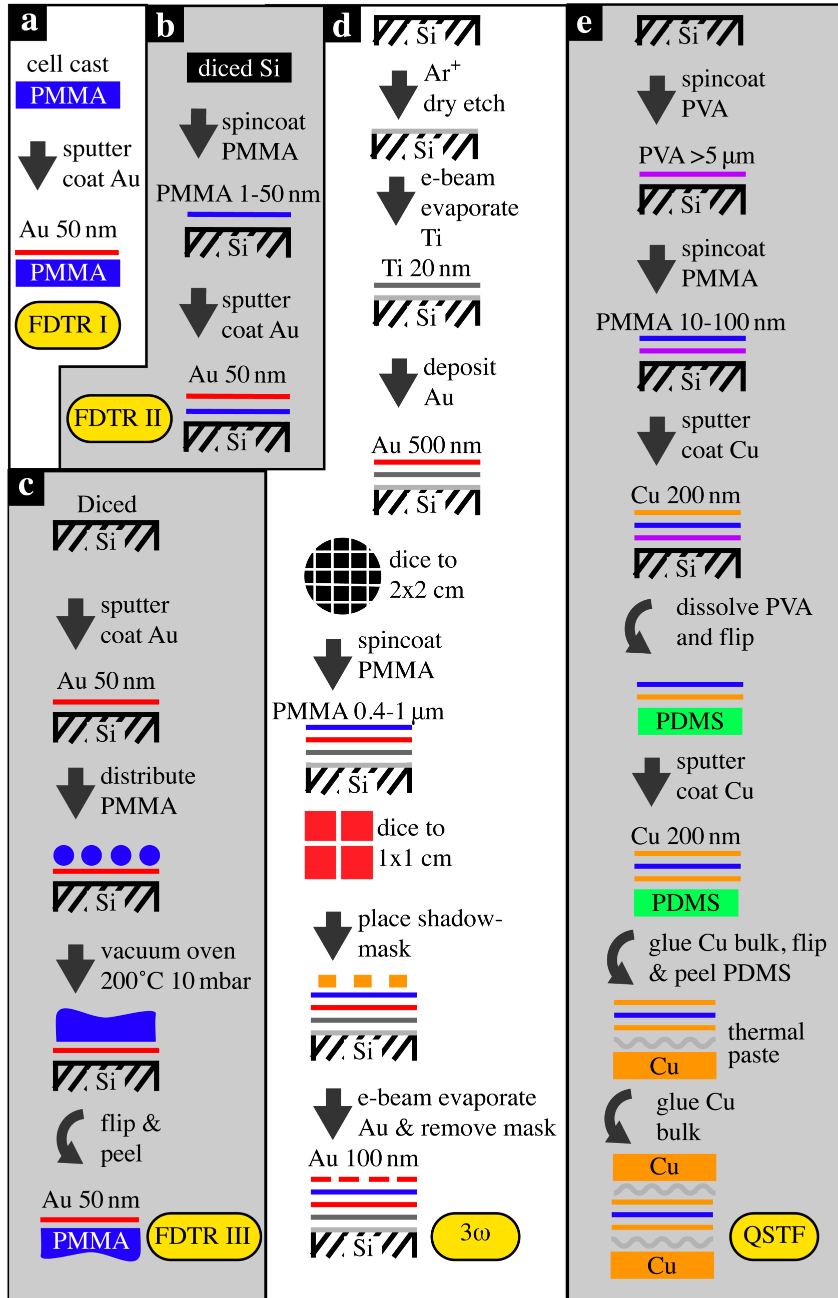

Figure 2.6. Overview of model systems and fabrication pathways. Models for frequency domain thermoreflectance (**a**-**c**), 3-omega (**d**) and quasi-static thermal flow (**e**).

2.4 Fabrication methods

Spincoating

Spincoating of polymer solutions is a fundamental technique of nanotechnology, providing an efficient and repeatable route to produce polymer films used as photoresists in photolithography or as permanent components of devices. Polymer solution is applied to the center of a level substrate mounted onto a rotating chuck. The chuck is accelerated to a certain speed, applying centripetal forces to the liquid, causing a spreading on the substrate and eventual discharge from substrate edges if radial forces surpass those of liquid surface tension. On the substrate, film formation is governed by solvent viscosity (ν_0), solvent evaporation rate (e), polymer concentration (c), polymer molecular weight ($\overline{M}_w$), spin speed (ω) and solution-substrate interactions, assuming the film to be dry upon completion of the spinning process [25]. The simplest model accounting for only changes in spin speed is the power law

$$L = A\omega^{-\alpha}, \tag{2.9}$$

where L is final thickness in nm, A is a constant and α is a constant commonly evaluated to 0.5. From a set of thickness values, A and α can be determined and the reverse formula

$$\omega = \left(\frac{L}{A}\right)^{-\frac{1}{\alpha}} \tag{2.10}$$

used to determine accurate spin speeds needed to achieve a given thickness.

From the value of α and a common ω range of 500-8000 rpm it is clear that the thickness can be varied by up to four times by spin speed only. For nanometer thickness films, other parameters prove more efficient to alter thickness. A in (2.9) comprises system parameters e, ν_0, c and $\overline{M}_w$.

$$L = \frac{3}{2}^{\frac{1}{3}} c(1-c)^{-\frac{1}{3}}\omega^{-\frac{2}{3}}\nu_0^{\frac{1}{3}}e^{\frac{1}{3}} \tag{2.11}$$

accounts for the most relevant terms [25], indicating that the reduction of all parameters e, ν_0 and c results in thinner films. When it is desirable to keep the same solvent-polymer combination, c presents itself as the parameter of choice once the change by spin speed has been expended.

Having already chosen PMMA as the polymer of interest, a literature review

reveals anisole as a suitable solvent. It has a low vapor pressure, yielding thinner films [26, 27], can dissolve PMMA of $\overline{M}_w$ 996 000 up to a concentration of at least 10 wt.% [28] and is less hazardous compared to other common solvents such as toluene and chloroform. (2.11) can be replaced by the power law

$$L = Ac^n\omega^{-\alpha} \tag{2.12}$$

or exponential variation

$$L = Ae^{nc}\omega^{-\alpha}, \tag{2.13}$$

where the latter was preferred for PMMA spun from three different solvents at concentrations from 1.2 to 6 wt.%[27].

Thin polymer films are vulnerable to a number of defects resulting from improper dispensing of solution, particle contamination, air bubble contamination and film tensile stress. In films <10 nm thick, tensile stress overcoming the material yield stress causes unavoidable formation of pinhole defects upon complete drying [29]. Complete drying can be achieved by storing in vacuum for 1 d [29]. Baking at a hotplate at 200 °C for 2 min was however not enough to cross the glass transition temperature and dry off all chlorobenzene solvent [29]. For thicker films in the 500 nm range, internal stresses can to a larger extent be accommodated inside the material and defects as a result of drying are not expected [30].

DC magnetron sputtering

Direct current (DC) sputtering of metals is a common process in most lithographic methods to rapidly deposit metal onto relatively flat substrates with good uniformity and possibility to build stacks of different metals to increase adhesion, as well as mechanical [31, 32] and conductive properties [33]. The basic sputtering setup is illustrated in Figure 2.7 and includes a rotating substrate holder, a metal target and an electric cathode, all inside a high vacuum chamber. After inserting a sample, the chamber is pumped to high vacuum to remove potential reactive gasses before introducing a partial pressure of a noble gas in the 0.1 to 10 mbar range. A DC field causes the (e.g argon) gas to discharge and form a plasma, which is maintained by the continuing emission of electrons from both target and cathode. Ions are accelerated towards the target by the electric field, and a collision cascade results in the ejection of high energy target atoms that in turn hit the substrate. While in flight, metal atoms

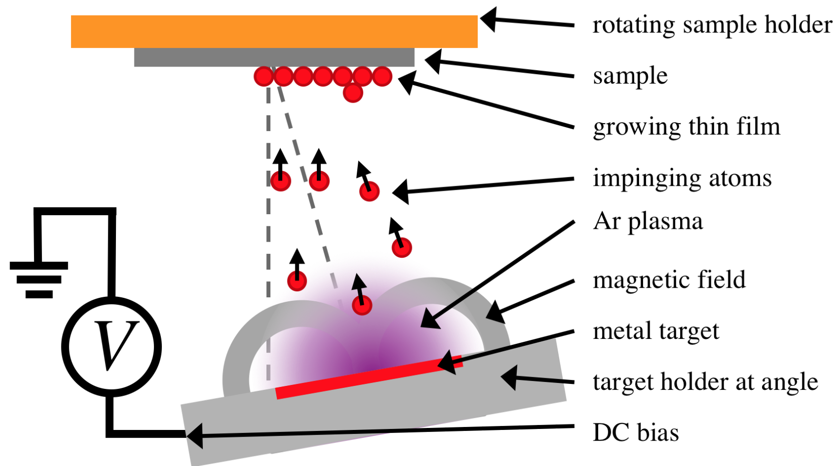

Figure 2.7. Illustration of a generalized DC magnetron sputter setup. The setup is placed inside a vacuum chamber.

lose kinetic energy in collisions with the gas, regulated by gas pressure. In magnetron sputtering, as used herein, plasma is maintained close to the surface of the target by a permanent magnet for higher sputtering rates and lower sample contamination. [34]

Near interface metal growth

The study of initial nucleation and growth behaviour for thin metal films on polymer substrates at or below the percolation threshold is pursued in the interest of improving molecular sensing devices and catalytic surfaces. The work of Ruffino et al. [35, 36] describes the growth of Au and Ag on poly(styrene) (PS) and PMMA substrates using atomic force microscopy (AFM). The authors further demonstrated and explained the effect of Ag and Au nanoparticle diffusion and embedding in the polymeric substrates at temperatures above the glass transition temperature. In particular, they found the rate of embedding to increase with increased metal-polymer wetting and that the process can be accurately described statistically as a process of full nanoparticle wetting followed by gradual embedding. The work of Kaune et al. on Au pulse sputtered on poly(N-vinylcarbazole) coincides with that of Ruffino et al. to establish the nucleation and growth process of incident Au atoms [35, 37]. This work on the growth process is later expanded upon by Schwarzkopf et al., first for Si substrates [38], later for PS [39] and lastly, the relation between sputter rate and morphology evolution is uncovered [40]. The growth model is comprised of four stages seen in

Figure 2.8a, including nucleation, lateral growth, coarsening, and vertical growth [37]. The main effects of higher deposition rate was lower initial particle size and decreased percolation threshold explained as an increase in polymer bonding from increased polymer damage with increased sputter energy [40]. This increased sputter energy was a result of increasing deposition rate while maintaining a constant Ar pressure. Both Kaune and Schwartzkopf use X-ray reflectometry (XRR) to demonstrate that the incident Au atoms embed down to ∼5 nm into the polymeric substrates [37, 39]. The same XRR data demonstrate the presence of a Au cluster layer on the metal surface, observed throughout literature studies and visualized using both scanning electron microscopy (SEM), AFM and cross-section scanning tunneling electron microscopy in [41].

These findings are important to understand the little accessible metal-polymer interface beneath sputtered metal films. However, the initial nucleation and growth stages are not necessarily coupled to the internal microstructure of >30 nm thick Au films. If the initial growth stages result in a continuous metal film with low roughness, the continued adsorption and growth will occur on metal sites and can thus be expected to be similar to growth on metal substrates.

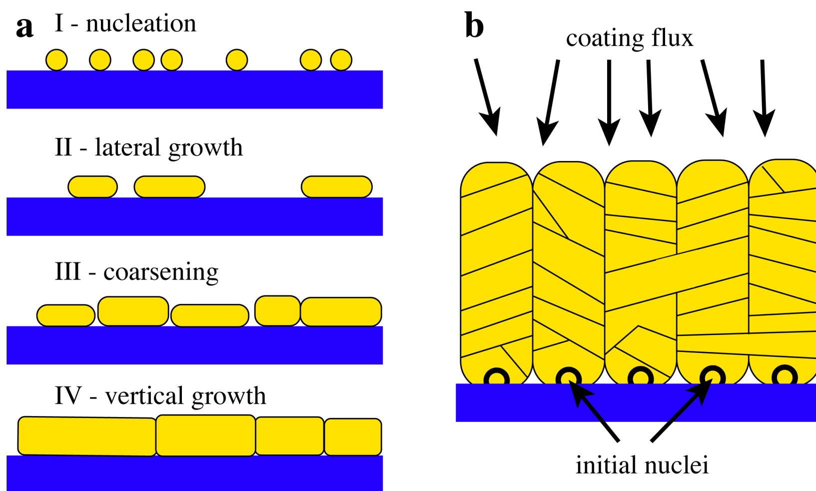

Figure 2.8. **a**, nucleation and growth model of noble metal films on polymer substrates. **b**, profile of columnar grains with scattered imperfections and predicted surface profile. **a** and **b** adapted from respectively, [37] and [42].

Grain growth in the metal bulk

Initial nucleation and growth affects all four interface properties mentioned in Figure 2.5, the continued growth determines the bulk and surface morphology and in turn thermal conductivity and heat capacity of the metal layer. Investigations into sputtering parameters and resulting film properties have been undertaken since sputtering was first used in fabrication, with the structural zone model (SZM) developed by Thornton emerging as the most accepted model for metal film growth by magnetron sputtering [34, 42]. The model describes how films grow into four different structures depending on temperature of the substrate relative to the melting temperature of the deposited metal (T_s/T_m) and gas pressure (P_{Ar}). To fully understand the sputtering process, it is, however, important to include even more parameters to uncover how T_s/T_m and P_{Ar} influence the microscopic movement of atoms. The parameters that can be varied in a sputter setup are substrate temperature, roughness and structure, deposition rate and angle as well as gas pressure, target bias and deposition time. This list of parameters is non-exhaustive as several modifications to magnetic fields, electrodes, target geometry and plasma confinement are possible [34].

Metal nucleation at low T_s/T_m is characterized by growth far below equilibrium conditions, governed by severely limited diffusion and low critical island size [32, 42]. Models and experimental studies of crystalline thin films grown at low substrate temperature reveal that films will assume a structure of columnar grains seen in Figure 2.8b, surrounded by either voids or amorphous phase material. To overcome surface diffusion barriers, incoming atoms must have sufficient energy, and as there is little thermal energy from the substrate, energy can only be increased by increasing the target bias or decreasing the gas pressure to minimize energy lost to gas collisions before reaching the substrate. Surface diffusion can also be increased by lowering diffusion barriers such as roughness and substrate-metal interaction energy. Depositing at an oblique angle will result in higher surface diffusion due to a higher lateral component of the incoming atom momentum. Oblique angle deposition can also cause anisotropic growth due to shadowing, where elevated surface features receive a higher portion of the incoming flux and thus grow faster [42]. A high flux of atoms will increase the amount of free atoms on the surface, thus shifting the growth further away from equilibrium as the atoms have less time to rearrange before new material is deposited [40]. In general, the average diffusion time is decreased for higher fluxes, leading to a more diffusion limited growth and lower density films.

In the SZM, for $T_s/T_m < 0.5$ the film will grow in either Zone I or Zone T,

the latter having the most desirable mechanical properties of the two [32]. Zone I is characterized by a tapered columnar structure appearing porous due to voids separating the columns. The voids are formed due to high diffusion barriers and a strong effect of shadowing from the growing columns. In Zone T, adatoms are able to overcome diffusion barriers and form the same fibrous grains, but embedded in an amorphous inter grain structure [32, 42]. Although far less pronounced, shadowing will still afford a spherical cap to the columns as seen in Figure 2.8b. To add energy without elevating substrate temperature, a bias can be applied to the substrate causing a bombardment of inert plasma ions. The added energy in what is called energetic enhanced deposition which enhances morphology control.

Metal grains are expected to grow in size with increasing film thickness [43]. Huang et al. observed poly-crystalline grain-like structures in 14-200 nm thick Au films on HCl-poly(aniline) pellets, which was attributed to the pulsed sputtering deposition used [43]. Using SEM and four-point probes, they observed increasing grain size and electrical conductivity with increasing thickness. A columnar structure of 1 µm Cu films sputtered on Kapton rubber is clearly visible in Figure 7 of [44] and Au film on SiO_2 in Figure 3 of [41]. Linear growth of grain size (d_g) with thickness (L) for grains appearing on the film surface was reported for 50-1000 nm Cu films as

$$d_g = 0.58L + 110\,\mathrm{nm}, \tag{2.14}$$

with the growth rate from 50 to 100 nm being slightly steeper [45].

Adhesion and transfer printing

Adhesion between metal and polymer is interesting as it is known to be important for TBC [8, 13]. The adhesive force between two materials is determined by the interface area, the nature and number of chemical or physical bonds and the presence of voids, defects or contamination in the interface [4], i.e. nearly all factors affecting TBC. For PMMA, no covalent bonds to transition metals can be expected as the only chemical groups present are methyl ($-CH_3$) and carbonyl ($-COOCH_3$) groups. The range of physical bonds available are thus limited to van der Waals bonding through dipoles or induced dipoles interacting with the electron sea of the metal [46]. In the more general case it is known that polar groups, π-bonding benzene rings and free radicals enhance metal bonding [47].

By studying the effect of various plasma treatments on five different thermoplastic

polymers, the amounts of free radicals and polar groups were found to be most significant for metal-polymer adhesion [48]. The effect of Ar and O_2 ion etching on the Cu-polymer interface was studied in detail for PS, bisphenol-A-polycarbonate, poly(α-methylstyrene) and PMMA by Zaporojtchenko et al. [47]. Similarly to Schwartzkopf et al. [40], they found that metal-polymer nucleation sites increased with increasing ion fluence, which was attributed to polymer damage from cross-linking, chain scission, formation of new functional groups, removal of old functional groups and creation and free radicals [49]. Adhesion failure at higher fluences was linked to the upper nanometers of polymer becoming severely damaged, causing this upper layer to break before the improved metal-polymer interface. It was also noted that PS showed the most dramatic increase in bonding strength, likely due to the higher amount of chemical species that can be formed by breaking benzene groups. A comparative study found that 20 nm e-beam evaporated Au adheres more strongly to silk protein than PMMA and that both substrates offered significant Au morphology improvements compared to Si and SiO_2 for 3-10 nm Au films [50]. Improved adhesion and uniformity was attributed to a high density of amino acid $-NH_2$ and $-COOH$ groups in the protein that adhered more strongly to Au.

Testing of interface adhesion can be done in absolute terms by for example 90° pull testing [47], shear strength testing [48], or the very simple comparative scotch tape testing [8]. Independent of chosen method, the fracture zone should be inspected to observe if there is any material remaining, which will determine whether the failure is adhesive (no material left), cohesive (material remaining), or a combination of the two. The scotch tape test can be very easily performed as a first check for adhesion by simply attaching a piece of tape to the surface and pulling manually. For a material stack, the weakest interface will naturally yield first, thus differences in interface structure between different fabrication routes or for different materials can be detected as a change in interface adhesion. The tape in use can be altered to allow tuning of the applied force.

One recent breakthrough allows the simple peeling and deposition of thin films or other nanostructures through the use of rate-dependent adhesion of silicon rubber in a process called transfer printing [51]. Due to its viscoelastic properties, the rubber, commonly poly(di-methyl siloxane) (PDMS), demonstrates strong adhesion when peeled rapidly and the opposite upon slow peeling, i.e. as slow as $<1\,\mu m\,s^{-1}$ [52]. Losego et al. fabricated thin film devices for TBC measurements by transfer printing a Au film onto self-assembled monolayers [13]. A poly(vinyl alcohol) (PVA) film was first spun onto the Au surface to impart mechanical stability during the transfer

printing process. PMMA can also be utilized to move nanomaterials of complex geometries by solution casting followed by peeling, printing and lastly dissolving PMMA is acetone vapour [53]. Evidently, the exploitation of interface-dependent adhesion can be of great help when fabricating laminar structures.

2.5 Characterization methods

Surface roughness

Surface roughness is a set of parameters used to describe the surface of engineering surfaces ranging from mirror-like to intentionally roughened. For model systems produced herein, surface roughness is a useful parameter to both verify that completed samples are sufficiently smooth and to detect surface changes between different fabrication steps. Different needs have given rise to a wide range of surface parameters [54]. The ones that will be mentioned in this thesis are mean squared roughness (R_q), surface mean squared roughness (S_q), and maximum peak-valley distance (S_z). In the following it is assumed that the mean ($\bar{z}$) of all measured points z_i is zero, easily afforded by vertically shifting the measured points by $z_i + min(z) - \bar{z}$. R_q is the legacy parameter denoted in discrete form by

$$R_q = \sqrt{\frac{1}{N}\sum_{i}^{N} z_i^2} \tag{2.15}$$

and used due to its simplicity. S_q is the 2D version of R_q, useful for more complex surfaces, and is given by

$$S_q = \sqrt{\frac{1}{MN}\sum_{y}^{N}\sum_{x}^{M} z^2(x,y).} \tag{2.16}$$

S_q and R_q are identical in the case of isotropic self-affine surfaces. Additional parameters are needed to describe repeating structures such as wave patterns or affinity for certain directions. S_q is also insensitive to outliers, thus S_z is introduced as the maximum peak-valley height difference of a surface, or specifically $|max(z)|+|min(z)|$. In the present text, S_z will be calculated from the mean of the five highest and five lowest points. The reader is referred to [55] for a more in-depth introduction to the statistics of surface roughness.

Another parameter that will be used in this thesis to characterize defects is *total*

displaced volume. Every defect is measured as a map of height values higher than or lower than two times the standard deviation of sample height distribution. For each defect, the displaced volume is then equal to the volume enclosed by the points in this map, which will be positive for peaks and negative for valleys. By summing these volumes, the amount and character of sample defects can be quantified.

Atomic force microscopy

AFM was first introduced by Binning, Quate and Gerber as a modification of their previous invention, the Scanning Tunneling Microscope, to allow it to sense forces in place of tunneling currents [56]. The modern AFM is based on piezoelectric crystals that moves the tip relative to the sample in the z direction, according to a feedback signal, while scanning in the x and y directions. The feedback signal is generated from a photodiode illuminated by a laser reflected off the cantilever tip and through a mirror as illustrated in Figure 2.9a. Thus, deflection of the cantilever beam resulting from proximity to the surface as the surface is moved in the xy-plane, is translated to vertical motion and height is recorded for every pixel in the map. Since its invention, many improvements and new modes have been conceived [57].

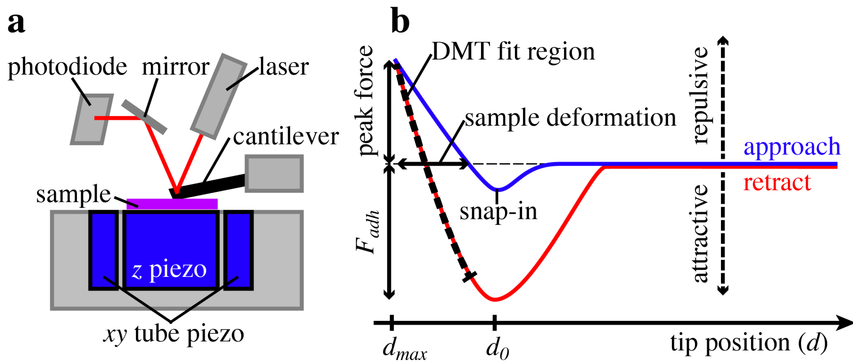

Figure 2.9. **a**, simple illustration of the an atomic force microscope with piezo stage. **b**, idealized force-distance curve obtained at each tap of the AFM cantilever with the source of different parameters indicated.

Inherent to all AFM modes are two potential hazards, namely tip convolution of the sample and sample damage. Tip convolution is the effect where a tip has either been dulled or has picked up part of the sample so that the shape and size of the tip has been altered. This alteration of the tip can lead to a decrease in vertical and

lateral resolution, multiple contacts with the same surface feature and convolution of surface and tip shape. Sample damage is also a problem if the contact forces exceed about 9 nN. Keeping both tip and sample interaction effects in mind is important to correctly identify artifacts when analyzing AFM maps. A simple method to mitigate problems is keeping the interaction force low and replacing the tip once artifacts start to appear [36, 58].

A recent innovation, patented by Bruker, is the PeakForce Quantitative Nanomechanical Mapping™ (PF-QNM) mode. Based on a combination of tapping and indentation, the AFM cantilever is actuated far below its resonant frequency, allowing it to rapidly respond to sensed forces. The force (F) is calculated from the cantilever spring constant (k) and a calibrated deflection sensitivity (S) measured as voltage change (D) in the photo diode per nanometer vertical movement to get $F = kSD$ [59]. From the crystal z-movement (z), the vertical tip position (d) is calculated as $d = z - SD$. Thus, with accurate calibration, force-distance curves like the one illustrated in Figure 2.9b can be captured for every contact point and used to extract useful mechanical properties. [59, 60]

Topography is directly extracted from the crystal z-position, regulated by the peak force feedback loop that maintains the sensed peak force on the software-controlled set-point. Sample deformation at each point is found from ($d_{max} - d_0$) through fitting to the points indicated in Figure 2.9b. Similarly, the force of adhesion between tip and sample (F_{adh}) is found directly from the negative force at the lowest point of the retract curve. Lastly, reduced modulus (E_r) is calculated by fitting the retract curve to the Derjaguin–Muller–Toporov (DMT) model

$$F = \frac{4}{3} E_r \sqrt{r \left(d - d_0\right)^3} + F_{adh}, \tag{2.17}$$

where r is the tip radius and $d - d_0$ is the deformation of the sample at any point d along the retract curve. The reduced modulus can then be converted to the elastic modulus (E_s) by

$$\frac{1}{E_r} = \frac{1 - v_s^2}{E_s} + \frac{1 - v_i^2}{E_i}, \tag{2.18}$$

assuming the tip modulus (E_i) to be infinite and knowing the sample Poisson's ratio v_s. Generally, Poisson's ratio is not known, so for this work it is approximated to 0.3 as suggested by the operating manual for samples with elastic modulus larger than 1 GPa. [59, 60]

Interference microscopy and optical profilometry

Interference microscopy is a non-contact technique for surface roughness and profiling applications. With custom optics, optical microscopes can be used to study interference patters generated by differences in light path from a beamsplitter to respectively, a sample and a reference mirror surface, illustrated in Figure 4.2a for a Mirau objective. Indeed, visual inspection has long been used to optically assess the quality of manufactured surfaces. Advancement of computers and CCD cameras during the 1990s opened the possibility to extract accurate values from interference data of large areas rapidly. The modern setup is equipped with advanced optics, hardware and software, automated vertical movement and varying degree of automation in focusing, xy-stage movement and tilt adjustment. [54]

Data interpretation can be split into two main categories, namely phase scanning interferometry (PSI) for smooth surfaces and vertical scanning interferometry (VSI) for rough or structured surfaces. PSI is based on interpreting the phase shift of a narrow wavelength light that has interacted with the sample, and calculating roughness based on known effects of roughness. It assumes that the whole surface is continuous and is generally limited to roughness of mirror-like finishes, approximately 30 nm. VSI, on the other hand uses broadband white illumination, where interference maximum only overlap for all wavelengths simultaneously at a narrowly defined vertical sample distance, which can be found by precise vertical scanning. Algorithms determine at which vertical height each pixel reaches this spot, allowing individual positioning of each pixel in vertical space creating a 3D image even for rough surfaces or surfaces with steep edges. [54]

Combining PSI and VSI is possible through clever measurement routines or algorithms and allows roughness of 3D structures to be measured at high precision [54]. Bruker has dubbed their combined method VXI [61], which will be referred to throughout this thesis. An interesting feature of optical profilometry is that both PSI and VSI can be used to characterize surfaces buried beneath smooth transparent films. The use for the planned model systems is obvious, in that it allows non-invasive characterization of interfaces between transparent PMMA and solid Au.

Thickness of thick transparent films is readily measured in VSI by the vertical separation of light reflected from the film-air and the substrate-film interfaces. For films thinner than about 2 µm, the fringes of both interfaces overlap and so the measurement of film thickness presents difficulties. One option is to use a reference substrate and knowledge of film refractive properties, called reflectometry. If an even

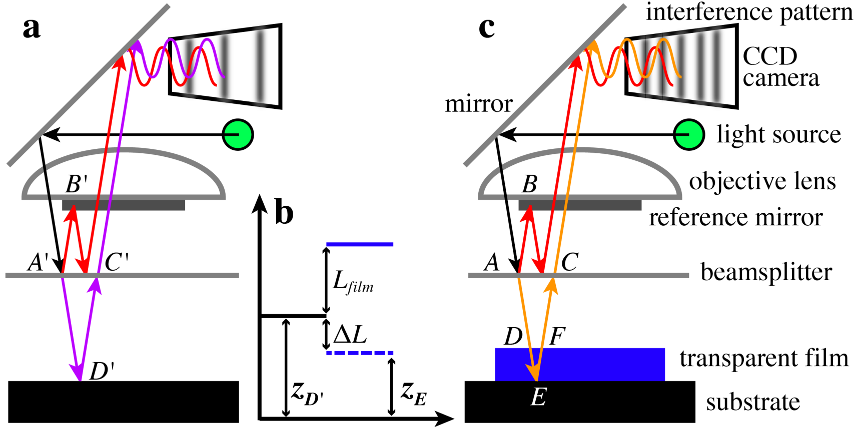

Figure 2.10. **a**,**c**, highly simplified optical configuration for a Mirau objective. Light path is indicated for the case of bare substrate (**a**) and transparent film thinner than 2 µm (**c**). **b**, step edge profile with substrate (black), apparent film surface (stippled blue) and actual film surface (blue).

step edge is present, the height of the film can be found from a VXI map, however with a small caveat: The transparent film is not recognized by the software, thus the longer travel time through the higher refractive index film is interpreted as a surface lower than the substrate. A correction is readily conceived using narrow wavelength light and some optical considerations. [62] From the simplified geometry illustrated in Figure 2.10a and c, the measured distance (z) of the two surfaces is

$$\begin{aligned} z_{D'} &= 0.5(A'B'C' - A'D'C') \\ z_E &= 0.5\left(ABC - (AD + nDEF + FC)\right), \end{aligned}$$

where $A'B'C'/2 = ABC/2$ is the known reference distance between the beamsplitter and the mirror and n is the refractive index of the film for the chosen wavelength. Noticing that $DEF = 2DE$, $AD = FC$, $A'D'C' = 2A'D'$ and $A'D' - AD = DE$, an expression for the difference in measured height can be found as

$$\begin{aligned} \Delta L = z_{D'} - z_E &= 0.5\left(2AD + 2nDE - 2A'D'\right) \\ &= AD - A'D' + nDE \\ &= (n-1)DE. \end{aligned}$$

Thus, the actual film thickness can be calculated by the simple expression

$$L_{film} = (n - 1)^{-1} \Delta L. \tag{2.19}$$

Stylus profilometry

The stylus profilometer is a contact method, where a normally diamond tipped stylus is moved with a set contact force, speed and distance along a line on the surface of a sample. The relative elevation is measured at regular intervals by a force transducer as the amount of vertical movement needed to keep the force constant. Features down to the nanometer scale can be measured, with resolution limited by sample properties, instrumental setup and vibrations. From the measured linear profiles, sample properties such as step heights and roughness can be determined. [63]

μ-Raman spectroscopy

Raman scattering is the result of light interacting inelastically with vibrational and rotational modes of molecules and crystals, first measured experimentally by Raman and Krishnan in 1928 [64]. Probe light in the visible or near infrared region excites molecular or lattice vibrations in the same energy range. The interacting light is scattered at a series of lower frequencies, corresponding to the amount of energy lost to the excitation. By accurately measuring the relative intensity of scattered light at every frequency, a fingerprint of the material can be formed, similar to infrared spectroscopy. The interpretation of this spectrum beyond qualitative purposes requires advanced theoretical models and is generally not afforded for complex multidimensional systems such as polymers. Quantitative data can, however, be easily acquired as the intensity of the signal is directly proportional to the amount of material in the interaction volume. Thus, after calibration, Raman spectroscopy can be used both to verify structure and to estimate concentration or amount of constituent compounds. [65]

All polymers have vibrational modes related to the orientation of the backbone. If the polymer is oriented, for example by intrinsic folding, mechanical stretching or extrusion, the carbon backbone will align and vibrations will occur preferentially in one direction. Polarized light has electromagnetic waves that only oscillate in one direction, thus only interacting with similarly oriented vibrational modes. Using μ-Raman spectroscopy, changes in orientation along the lateral dimensions of a sample can be mapped, which is interesting for semi-crystalline materials and materials

with anisotropic direction of polarization. During spincoating, polymer solutions experience both high centripetal acceleration and continuous removal of solvent causing an increase in viscosity and polymer-polymer contact. Like in extrusion or injection moulding processes, some alignment of the polymer backbone is therefore expected. Using polarized μ-Raman spectroscopy, such molecular orientation should manifest as a difference in intensity of spectra acquired with polarization parallel or perpendicular to the radial direction. [66]

Field emission scanning electron microscopy

In SEM, a sharply focused electron beam raster scans a surface to form an image based on information gathered at each pixel. SEMs equipped with a field emission gun (FE-SEM) have smaller beam size and higher current density at low voltage operation and are therefore preferred in the study of poorly conducting samples. The scanning beam interacts with the sample at every pixel according to the scattering properties of the incident beam and subsequent radiation from the sample. Commonly, electron-sample interactions are though to occur in an onion-shaped volume where secondary electrons are emitted from the surface, and X-rays and backscattered electrons (BSE) are emitted from the bulk. Secondary electrons are emitted more frequently from higher points and edges affording the high vertical contrast seen in SEM images. When attempting to image layered materials, high acceleration voltages will cause multiple layers to be imaged simultaneously due to the interaction volume being larger than the topmost layer. BSEs can be used to create material contrast as they are more sensitive to atomic number and density of the sample, which can be useful for extremely flat samples. Exited X-rays can also be analyzed to determine material composition of the specimen, albeit only accurately for atoms heavier than carbon and with significantly reduced resolution due to the higher escape depth and interaction volume of X-rays. [34]

3

Materials & Methods

This chapter begins with general materials and procedures. Next comes details on film fabrication and characterizations using the optical profiler and AFM. Sample fabrication for 3ω , FDTR I and FDTR II models only describe methods, while the last fabrication section on FDTR III and QSTF is written to emphasize the material exploration performed for these samples. Some repetition will be observed, especially in washing and metal coating steps, as minor differences may occur. Last is presented methods for µ-Raman spectroscopy, adhesion testing and FE-SEM, which are not part of process optimization as opposed to previously mentioned characterization methods.

3.1 Materials

Cell-cast poly(methyl methacrylate) PMMA sheets of nominal thickness 1.1 mm and estimated mass average molecular weigh ($\overline{M}_w$) 500 000-1 000 000 (referenced to as 750k) were acquired from Goodfellow Cambridge Ltd. Grinded PMMA powder of $\overline{M}_w$ 120 000 as measured by gel permeation chromatography and Poly(vinyl alcohol) (PVA) 99.5 % hydrolyzed of unknown $\overline{M}_w$, was obtained from Sigma Aldrich GmbH. Anisole 99 % was acquired from Merck KGaA, and the container had been open for three years before the start of this project. All deposited metal was of $>$99.99 % purity. 4 in Si wafers were acquired from UniversityWafer Inc. Wafers with thermally grown SiO_2 were of unknown origin. Si wafers are always covered

by natural oxide (SiO_x) except in the case of 3ω models where the oxide is removed by dry-etching prior to metal deposition.

Dissolving PMMA in anisole

Sample bottles were cleaned in IPA, blow-dried and washed thrice in small amounts of anisole to yield a wet bottle. The weight of anisole wetting the bottle was noted. Washed PMMA sheets or untreated PMMA powder was added to prescribed weight before anisole was weighed in to yield desired concentration. Solid PMMA was dissolved using a combination of stirring and ultrasonic baths over the course of maximum two weeks depending on concentration and time spent resting on shelf. Due to the low flash point of anisole, care was taken to avoid heating during this process. Some solutions were passed through a 1 µm syringe filter, but no effect of this treatment was later noted. For simplicity, produced samples are named by $\overline{M}_w$ - wt.% (e.g. 750k PMMA - 5 wt.%). All solutions were made using PMMA dispersed in anisole.

Calibrating sputter deposition rates

The AJA International Inc. combined sputter/e-beam system used in this thesis work was only equipped with an in-situ thickness monitor for e-beam deposition. For sputter deposition, a quartz crystal microbalance (QCM) was manually moved into the sample position and metal thickness after 60 s deposition was noted for the desired sputtering power. The measured deposition rate was assumed to be accurate for subsequent film depositions. However, sputter targets were frequently changed, so deposition rate was measured every time the desired target material had been moved.

3.2 Spincoating PMMA on test substrates

To develop proper spincoating routines for PMMA solutions and verify the expected thickness and morphology of the spun films, a series of test spins were performed on Si and Au-coated Si substrates. Si wafer chips were cleaned in IPA, O_2 plasma for 1-3 min and dehydration baked on a hotplate at 180 °C for 5 min before spincoating up to eight samples in series at various times, spin speeds and accelerations for the different steps of Table 3.1. Annealing on a hot-plate at 180 °C for 2 min was performed for all samples to remove remaining solvent and relieve film stress. It

was found that solutions of <5 wt.% readily covered the entire substrate, allowing for omitting distribution spinning, while solutions of higher concentration required distribution and lower acceleration to max speed to avoid swirl pattern defects along edges. Films thicker that about 500 nm still had changing interference patterns after 60 s of spincoating, and were therefore allowed to rest on a flat surface until film color became uniform as exemplified in Figure 3.1. Later, resting was performed while spinning at 250 rpm to ensure uniform gravity pull.

Table 3.1. Spincoating program used to prepare 3ω samples.

Intention	Time /s	Set speed /rpm	Acceleration /rpm s^{-1}
Distribute solution	5	500	200
Spincoat	60	800-8000	2000
Drying	30-180	250	1000

3.3 Problems of film thickness measurements

The accurate measurement of films thinner than 2 µm is challenging. A reflectometer was available for non-destructive measurement of films >200 nm, but proved challenging on highly reflective Au-covered substrates. Although each scan in the reflectometer is fast, the exact point of measurement cannot be determined and sample moving is manual, making it comparatively slow when handling a large set of samples. An interference microscope (optical profiler), a stylus profilometer and an AFM was the three other readily available options, all requiring a step edge for thickness measurements. Steps are normally produced in one of two ways:

- Patterning by photolitography, followed to selective film removal by a developer solution.
- Scraping with a sharp tool such as a scalpel or a plastic tool.

Scraping with both scalpel and cocktail sticks were rapidly proven to damage underlying metal films. Furthermore, the optical profiler software did not correctly interpret the sharp, rough edges created by this method. On the other hand, patterning by photolithography is too time-consuming, especially for a large set of small samples with varying geometries. Thus a new method was invented herein, where one side of the film-covered chips was immersed in a solvent (acetone). In the simple setup pictured in Figure 3.1, multiple sample chips are attached to the bottom of a glass

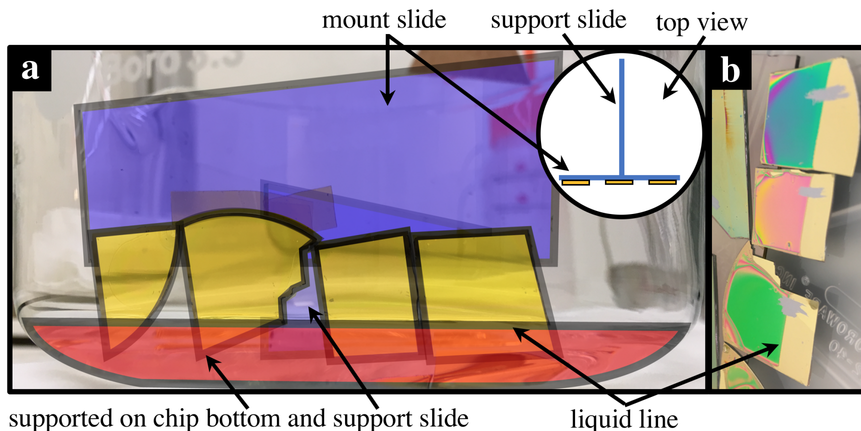

Figure 3.1. a, photograph of step fabrication in a bath of acetone. Translucent colors are have been added for glass (blue), samples (yellow) and solvent (red). Insert gives a top-view of the setup. **b**, photograph of PMMA films ~500 nm thick, coated on Au-covered Si wafer chips after step edge fabrication. A scratch made by a scalpel is also visible on each chip.

slide with double-sided tape. Another glass slide is attached perpendicular to the first slide, about level with the chip bottoms when viewed from the front. Care must be taken to ensure the solvent line remains on the same level and that it does not come in contact with the tape, which would then lose its adhesive, causing samples to fall into the solvent.

Vertical scanning interferometry to find polymer film thickness

Sample chips were attached by double-sided tape to the edge of a glass slide and lowered into a beaker as seen in Figure 3.1. The beaker was carefully filled with acetone from a squirt bottle to put the liquid-air interface at the center of the samples. Samples were left in the solvent for 3-10 min to completely dissolve the polymer layer before removing from the solvent by tilting the beaker in one smooth motion observing instant evaporation from sample surfaces. Samples were generally kept mounted to the glass slide as a convenient array for batch characterization.

Software-enhanced vertical scanning interferometry (VXI) on a newly acquired Bruker Contour GT-K optical profiler was used to measure step heights in the accompanying Vision64™ software. Samples were put on the sample stage and tilt manually adjusted to have three to five fringes perpendicular to the step edge. This choice of fringe orientation ensures that sample tilt is mostly parallel to the step edge,

simplifying tilt removal. Green (540 nm) narrow wavelength light was used to scan ±5 μm through the sample plane with the step edge located close to the middle of the field of view. Both a 2.5x and a 20x objective were tested at a combination of field of view (FOV) lenses of 0.55x to 2.0x to find the optimal balance of vertical resolution and FOV. For properly created step edges on smooth surfaces and objective and lens combination 20x + 0.55x, built-in algorithms for irregular step height detection could amply detect differences in light path length for the partly coated surfaces, allowing automatic measurement at evenly spaced points along the step edge. The irregular step height algorithm is based on finding the two maximums of the measured height distribution histogram. As described in Chapter 2.5, measured path length differences were subsequently transformed to height differences according to (2.19) using the refractive index of PMMA of 1.49. Thickness measurements from uneven step edges or thickness values deviating by more than 30 % from the spin curve were discarded.

Vertical scanning interferometry on metal films

Weakly adherent Au films were removed by Scotch tape while Au films strongly adherent to the substrate, i.e. with a Ti adhesion layer, were removed by scratching with a scalpel. Thickness as measured in the VXI mode was used without further adjustments.

Stylus profilometry for polymer films

A Veeco Dektak150 stylus profilometer was used to verify polymer film thicknesses measured by VXI. The diamond stylus had nominal radius 6.5 μm and was set to 30 mN contact force. In 'hill mode', the stylus was first lowered to the sample surface before scanning perpendicularly over the step edge at a scan speed of 0.025 mm s^{-1} with a total scan length of 500 to 1000 μm. Acquired data were subsequently leveled to the substrate tilt and height difference was recorded on areas of the curve close to the step edge. In the case of severe roughness, the baseline was put at the bottom of the first valleys visible after the step as seen in Figure 3.2b.

AFM for polymer films

The above mentioned methods were limited to films thicker than 150 nm, thus a Bruker Multimode 8 AFM with a PF-QNM upgrade was used to measure step heights for thinner films. Step edges for thin film samples on Si substrates were prepared using a sharp plastic cocktail stick. Instrument limitations caused the edge to only be

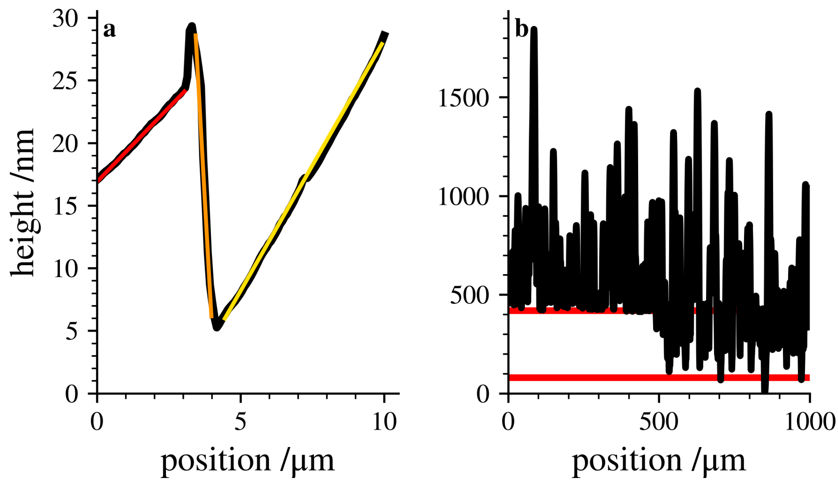

Figure 3.2. **a**, surface profile by AFM with superimposed fits of film, slope and substrate lines. **b**, rough surface profile for 3-omega samples of type E by stylus profilometry. Red lines indicate manual fits to film and substrate.

measurable in a region around the center of the 1 cm × 1 cm samples. Heigt maps were captured in the peak-force based ScanAssyst™ mode where all parameters except scan size and scan speed are controlled by the accompanying NanoScope™ 8.15 software using a Bruker ScanAssyst-Air tip of nominal spring constant and tip radius of respectively, 0.4 N/m and 2 nm. As only thickness was needed, calibration of deflection sensitivity, tip radius and spring constant was omitted. Force-distance curves were monitored to ensure stable behaviour. After capturing height maps, all lines were averaged parallel to the step edge, followed by fitting of the film, slope and substrate profiles as illustrated in Figure 3.2a. The height difference between the cross-sections of film and substrate lines with the slope line was taken as the film thickness.

3.4 Surface morphology measurements

For rapid, large-area determination of surface roughness and morphology, optical methods are clearly faster than contact methods such as AFM and stylus profilometry. With an automated sample stage and software optimized for large batch data capture, the Contour GT-K optical profiler can measure large portions of sample area in

minutes. However, manual alignment of stage tilt is still required for each sample unless completely flat. All data was captured in a 20x + 0.5x objective configuration yielding a net magnification of 11.1x. The optical profiler was used to find three different types of data: surface roughness of substrates, surface roughness of substrates or metal coating through transparent PMMA and defects and contamination present in, under or on top of PMMA thin films.

Roughness by phase scanning interferometry

As prepared samples and substrates were scanned in the Bruker Contour GT-K in the PSI mode using green (540 nm) light after adjusting tilt to obtain 3-5 vertical fringes. A total of 16 areas were scanned in a 4×4 grid, and surface roughness data captured automatically for each area.

Contamination and defects by phase scanning interferometry

Si/Au/PMMA(400 to 900 nm) samples prepared for the 3ω method were scanned as described above. In addition, a topography mask was applied to each scan to isolate regions higher or lower than about two times the standard deviation of the Gaussian height distribution. These regions were defined as peaks and valleys and their total displaced volume was calculated by the software. Areas with either S_q, S_z or total displaced volume outside of 3 times standard deviations were defined as outliers and removed. From visual inspection, such areas were generally distorted by large pin-holes or concentrated debris of for example Si dust from sample dicing.

Surface morphology by AFM

Nanomechanical mapping was performed in PF-QNM mode on the mentioned Multimode 8 AFM. All surfaces were mapped using a Bruker RTESPA Si probe with nominal spring constant and radius of respectively, 40 N/m and 8 nm. Before every use, the setup was calibrated on a clean sapphire surface to find deflection sensitivity, and on a poly(styrene) standard with 2.7 GPa elastic modulus to find approximate tip radius. As is clear from Chapter 2.5, having accurate D and R is important to get accurate modulus and deformation readings. Poisson's ratio was maintained at the software standard of 0.3. While not measuring accurate modulus, all controls were automatically varied by the NanoScope™ 8.15 software to give optimal maps with user defined mapping size and scan rate, thus most collected material property data are not accurate in terms of absolute value. Obtained maps were subsequently

flattened using Nanoscope Analysis™ 1.5 to remove 0th order line differences and 2nd order bow in larger scan size maps. Map color limits were subsequently set to three times standard deviation to obtain acceptable color contrast in the case of isolated peaks or valleys.

Double-sided surface morphology

One 100 nm Au film sputter coated on a PMMA sheet was peeled from the substrate by pressing onto a double-sided tape fixed to an AFM sample magnetic disk and removing the substrate with tweezers. The Au film had rested on shelf at room temperature (RT) and controlled relative humidity of 25 % for three months before inspection. Height maps were captured as described in Chapter 3.3.

3.5 Fabrication of 3-omega samples

Three sets of samples for 3ω were fabricated according to Figure 2.6d. Dry etched Si substrates were coated with a Ti adhesion layer before depositing a Au thin film using either e-beam evaporation or DC magnetron sputtering. Half of the samples coated with sputtered Au were coated with an uneven layer of carbon before 750k PMMA - 5 wt.% was spuncast onto all samples. Below follows the more detailed steps, where the three sets of samples are named S, SC and E for sputtered Au, sputtered Au with carbon and e-beam evaporated Au.

Table 3.2. 3-omega sample naming

Name	Substrate	Au deposition	Batch
S	SiTiAu	sputter coating	2
SC	SiTiAuC	sputter coating	2
E	SiTiAu	e-beam evaporation	1

Two as-received 4 in Si wafer were washed in isopropyl alcohol (IPA) and dried in a stream of N_2 before mounting into an AJA magnetron sputter/e-beam system. The AJA coater uses a rotating sample holder, with sputter target placed at an angle of 10°, 20 cm from the substrate. The e-beam crucible is placed directly opposing, 45 cm from the substrate. After pumping to base pressure of 1×10^{-7} mTorr, wafers were dry etched in 30 mTorr, 67 sccm Ar pressure at 25 W forward RF bias for 5 min to remove native silicon oxide. E-beam deposition of 20 nm Ti was performed at

8.9 kV and 58 mA to maintain a preset deposition rate of 5 Å s^{-1}. 500 nm Au was subsequently deposited on samples of type S and SC using DC sputtering at 3 mTorr, 540 V, 565 mA to yield a deposition rate of 5.85 Å s^{-1}. 500 nm Au was deposited on samples of type E using e-beam evaporation in two steps of 250 nm, both steps at 8.9 kV and 52 mA to yield a preset deposition rate of 5 Å s^{-1}. E-beam deposition was performed in two steps to avoid potential adverse effects of long deposition times such as QCM overheating.

After resting for 2 days, wafers were cut to 2 cm × 2 cm chips using a scriber to accommodate five different polymer film thicknesses and an uncoated reference sample for each of the three sets of samples. Samples of type SC were coated with an approximately 1.7 nm thick uneven layer of carbon in a Cressington Scientific Instruments Ltd. 208Carbon coater. To determine required spin speeds, a set of Si wafer chips cleaned in IPA, O_2 plasma and dehydration baked at 180 °C for 5 min were spincoated with 750k PMMA - 5 wt.% before softbaking at 180 °C for 2 min to yield the spin curves seen in Figure 4.4.

To remove carbon contamination prior to spin coating, samples of type S and E were cleaned in an oxygen plasma cleaner for 3 min. All samples were dehydration baked on a hotplate at 180 °C for 5 min and dust removed in stream of N_2 immediately before spincoating.

PMMA thin films were spuncast from 750k PMMA - 5 wt.% in a SÜSS LabSpin coating system using the program detailed in Table 3.1 with max speeds and drying times determined by the spin curves and time to form stable interference pattern, respectively. Samples of type E were spun to target thicknesses of 900, 750, 600, 500 and 400 nm at 865, 1411, 2571, 4198 and 7647 rpm, respectively. Samples of type S and SC were spun to target thicknesses of 800, 700, 600, 500 and 400 nm at 956, 1246, 1693, 2433 and 3791 rpm, respectively. Immediately after spinning, chips were softbaked on a hotplate at 180 °C for 2 min. After completing all spincoatings, samples were loaded into a vacuum oven and dried at 55 °C and 10 mbar pressure overnight. Finished samples were cut to (1 × 1) cm pieces before being placed in 4 × 4 chip-trays, covered with a clean-room wipe and packed in a N_2 filled zip-lock bag before shipping to Spain for thermal characterization. Note that uncoated reference samples for the two types of gold films received the same baking and drying treatments as the samples with PMMA thin film.

3-omega wire deposition

The last step of fabricating the thin film wire and breakout pads required for 3ω fabrication was not performed as a part of this thesis work, but is outlined here for completeness. After shipping from Norway to Spain, samples were placed under carefully cleaned shadow masks and loaded into an AJA e-beam coating system. After pumping to base pressure of 1×10^{-7} Torr, 100 nm Au was deposited at 1 Å s^{-1}. The deposited metal wire was subsequently inspected under a 100x objective to accurately determine heater width ($2b$).

3.6 Fabrication of FDTR I samples

PMMA sheets were diced into (1×1) cm pieces, washed in deionized water and dried on a hot-plate at 90 °C for 10 min. Samples were fastened to quartz glass slides with double sided tape and inserted into the AJA sputter coater and subsequently sputtered with 100 nm Au at 3 mTorr Ar pressure, 67 sccm Ar flow and 100 and 300 W power to yield deposition rates of respectively 0.95 and 5.3 Å s^{-1}. DC bias and current were automatically varied to maintain a stable output power. Previously, 5 to 50 nm Cu covered samples had been fabricated, which are mentioned in Chapter 5.6 and further detailed in [1].

3.7 Fabrication of FDTR II samples

Five samples were prepared for FDTR characterization: Si-carbon-PMMA-8000 rpm, Si-carbon, Si-PMMA-8000 rpm, Si-PMMA-4000 rpm and a Si reference sample. Si chips from a diced wafer were cleaned in IPA, dried in a stream of N_2 before a 3 min oxygen plasma clean. Two chips were coated with carbon simultaneously as the samples described in Chapter 3.5 to yield identical carbon layers. All samples were dehydration baked on a hotplate at 180 °C for 5 min. One carbon-coated sample and two clean samples were coated with 750k PMMA - 1 wt.% in a SÜSS LabSpin coating system, accelerating at 1000 rpm/s and holding max speeds of 4000 and 8000 rpm for 60 s. Immediately after spinning, chips were annealed on a hotplate at 180 °C for 2 min. After completing all spincoatings, samples were loaded into a vacuum oven and dried at 55 °C and 10 mbar pressure over night. After cooling, all five samples were mounted in an AJA sputter/e-beam system and coated with 50 nm Au using DC sputtering at 3 mTorr 530 V, 570 mA to yield a deposition rate of 5.85 Å s^{-1}. Duplic-

ate samples of Si-PMMA-4000 and 8000 rpm were kept without Au for thickness measurements.

3.8 Fabrication of FDTR III and QSTF model systems with concurrent adhesion testing

Initial investigations revealed several areas of improvement for QSTF and FDTR models [1]. For QSTF models, it was clear that any Cu bulk surface that was not highly polished would be too rough for spincoating a $<$100 nm thick polymer film. Polishing was deemed undesirable due to the likelihood of particles from the lubricant and mechanical shear forces to alter interface properties. FDTR model systems I and II where polymer sheets are sputter coated with metal had already proven successful. Now, it was desirable to alter fabrication method to accommodate more interface films and to vary polymer bond strength.

Towards FDTR III samples

For FDTR samples, polymer fabrication methods of interest include spin coating, casting from solution and casting from melt. It would be interesting to see if these methods could provide usable adhesion and if they could be more gentle to the polymer compared to the energetic sputtering process. To fabricate a polymer bulk ($>$500 µm) sample with a flat reflective coating analogous to FDTR I, it is necessary to create the thermoreflective layer first, coat it with polymer and remove the substrate to reveal the reflective coating. Thus, a substrate-metal film combination is needed that allows peeling of the metal film from the substrate. The substrate could also be chosen to withstand the heating needed to improve film density by moving the growth mode from zone T to III of the SZM.

Initially, Al was studied as an alternative to Cu, which was targeted due to its relevance for the microelectronics industry. It was quickly realized that Al had strong adhesion to Si substrates. Au is, however, known to have weak adhesion to SiO_2 [13], and this was proven to be true both for thermally grown SiO_2 and Si wafer chips. The same poor substrate adhesion was observed for Cu, with the thermally grown SiO_2 yielding a more uniform film as can be seen by comparing Figure 3.3a and b. At this point it became clear that the thermoreflective properties of Cu would require the use of two-color FDTR [67], which was not available. Thus, it was conceived to use a Au/Cu stack to obtain both Au thermoreflective properties

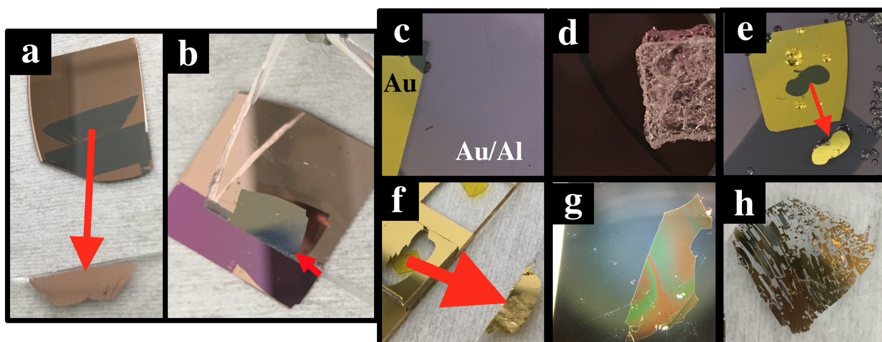

Figure 3.3. Comparison of peel tests, polymer melting and transfer printing results. **a**,**b**, Cu films peeled by PDMS slabs from Si and SiO_2 substrates, respectively. **c**, Au-Al alloy formed by heating of an initially laminar structure compared to pure Au as indicated. **d**,**e**, results of melting $\overline{M}_w$ 750k and 120k, respectively with subsequent peeling in the latter as indicated by arrow. **f**, Au film peeled from bulk PMMA substrate by PDMS slab. **g**, PMMA-Au laminate being transfer printed to a Si substrate as seen through a microscope. **h**, fractured Au film after unsuccessful transfer printing.

and the interesting Cu/polymer interface. Initial trials with Al proved Au and Al to alloy at temperatures as low as 60 °C. The alloy color turned a shade of purple seen in Figure 3.3d and adhered strongly to Si substrates. Without heating, the crucial dehydration and annealing steps of the spinning process could not have been performed, not to mention the >400 °C needed in any metal annealing steps. As the same alloy effect is expected for the Au/Cu system [68], the double metal idea was discarded and a pure Au film was pursued. A possible route for lowered adhesion that was not explored is that of Barrier et al. where a glass slide or Si substrate is coated with a low surface energy organic film prior to metal sputtering to lower surface tension and permit peeling of metal films [69].

Sputter coating and spincoating are mainly relevant for diode and other organic electronics applications. For bulk composite materials, the interface is most likely to be formed in a melt or partly polymerized state [48]. It was therefore endeavoured to melt PMMA onto a Au coated Si substrate to make a polymer bulk with Au transducer for FDTR characterization. The first attempt proved cell-cast $\overline{M}_w$ 750k PMMA to not be meltable as seen in Figure 3.3d, likely due to its high molecular weight. Si chips from a diced wafer were cleaned in IPA before mounting in the AJA sputter/e-beam system. After pumping to base pressure of 1×10^{-7} mTorr, wafers were coated with 100 nm Au using DC sputtering at 3 mbar and 300 W to yield a

deposition rate of 5.2 Å s^{-1}. As-received $\overline{M}_w$ 120k PMMA was melt cast onto the Au coated Si chips in a vacuum oven at 200 °C and 10 mbar pressure for 16 h before releasing pressure and cooling to RT. Isolated polymer islands were subsequently peeled together with the Au film from the Si substrate with the aid of tweezers as exemplified in Figure 3.3e.

Towards QSTF samples

Samples for QSTF studies were imagined to be a novel structure with a Cu film on both sides of a PMMA film thinner than 100 nm as illustrated in Figures 2.3 and 2.6e to alleviate the aforementioned roughness issues. The metal film should be applied by the same method on both sides to produce two identical interfaces, doubling the amount of measurable TBC. Clearly, a solution can not be spincoated onto two opposing metal surfaces simultaneously, thus sputter coating of metal onto PMMA must be the method of choice. To achieve a double coating, a film is spun onto some substrate, coated with Cu on one side, peeled from the surface and lastly coated with metal on the other side.

A substrate that permits peeling of a spuncast PMMA film is needed to achieve this model system. Although initial tests with drop-cast PMMA films yielded promising peeling results, spuncast PMMA demonstrated strong adhesion to both Si and week-old Al-sputtered substrates. For freshly sputtered Al films, PMMA solution was simply ejected from the substrate and no continuous film was formed. Thus, it was demonstrated how adhesion between film and substrate is a prerequisite for spincoating, and having a substrate from which PMMA can be peeled without chemical changes [53], appears to be a paradox. Scotch tape adhesion testing of Au sputtered on PMMA bulk substrates as seen in Figure 3.3c, made it evident that the Au-PMMA bond was weaker than the Cu-PMMA bond from FDTR I samples, which only rarely yielded any metal to the tape. The sputtering process, especially at high deposition rates, is believed to impart damage on the polymer film through chain scission, cross-linking, reaction with side groups, deforming of polymer surface and metal embedding into the polymer bulk [49], which should yield a stronger metal-polymer adhesion than any low-energy process. The peeled spuncast PMMA-Au laminate shown in Figure 3.3g, was therefore believed to be able to yield free-standing PMMA by removing the Au film. Attempts at separating the Au and PMMA yielded, however, only Au fragments and a highly fractured film, similar to that of Figure 3.3g. PMMA films from 3ω samples, where the Au film was strongly adherent to the substrate due to the Ti adhesion layer, neither film yielding any material to the scotch

tape. Thus, it is clear that stronger interface adhesion is achieved by spinning PMMA on Au than by sputtering Au on PMMA, contrary to initial assumptions. No samples were therefore fabricated, but a novel release layer was developed as a continuation of this work as detailed in the following section.

3.9 Water soluble release layer

To circumvent the paradox of spincoating on a removable substrate, a new procedure was needed. Losego et al. used a spuncast PVA film when transfer printing a Au film from SiO_2 to improve film mechanical stiffness [13]. PVA was subsequently removed in a stream of water. Thus, the idea was born to use a PVA film as a water dissolvable layer in between Si chips and PMMA to facilitate gentle removal of the substrate.

Disposable glass bottles were washed in IPA, dried in a stream of nitrogen, weighted and subsequently washed in DI-water. After obtaining the weight of remaining water, PVA was weighted into the beakers, sufficient to make 10 mL solution with concentrations of 5, 10, 15, 20 and 30 wt.%, before an exact volume of water as calculated from the actual polymer weight was added by a micropipette. The polymer was completely dissolved by a combination of repeated ultrasonication, magnetic stirring, vigorous shaking and heating to 75 °C in a water bath. The largest reduction in solids was observed during heating steps.

Si chips were washed in IPA and dried in a stream of nitrogen before spincoating as detailed in Table 3.3 and drying on an aluminium-foil covered hot-plate set to 100 °C for at least 5 min. 750k PMMA - 1 wt.% and 750k PMMA - 8 wt.%/ were subsequently spun on two PVA-covered chips using the same program, but omitting the distribution step. After drying, the two PMMA-covered samples and one reference sample without PMMA were attached to PDMS slabs by gentle pressing. The slabs were subsequently placed in DI-water, fixed above the surface by glass slides as seen in Figure 4.15a and left overnight to dissolve PVA.

Table 3.3. Spincoating program used to prepare PVA samples.

Intention	Time /s	Set speed /rpm	Acceleration /rpm s^{-1}
Distribute solution	10-20	500	200
Spincoat	120	2000	500

3.10 µ-Raman spectroscopy

µ-Raman spectroscopy was performed using a Renishaw inVia™ Raman spectrometer with a 532 nm laser using 50x and 100x objectives focused on the sample surface at various laser intensities and exposure times. The broad range of electron energy transitions possible in metal films saturate the Raman spectrum for all frequency shifts, thus only polymer bulk, Si or SiO_2 can be used as substrates. A pin-hole was used for some thin-film samples to lower the depth of field and thus limit substrate signal. When attempting to evaluate the degree of polymer orientation, a polarization filter was inserted in the illumination beam. Spectra were captured in the accompanying Wire 4.1 software, where spurious cosmic ray peaks were removed followed by baseline removal through an implementation of asymmetric least squares smoothing algorithm [70] before plotting.

Carbon content

To verify the presence and composition of carbon evaporated onto some of the of 3ω and FDTR II samples, µ-Raman spectroscopy of the carbon coating on a SiO_2 substrate was performed. The region around D and G bands (800-1940 cm^{-1}) proved to be clearly characteristic of the presence of carbon, thus this region was used to make a random map of 10 different points to verify the omnipresence of carbon. All samples were coated with carbon in the same batch, these results are therefore expected to be valid for all sample.

3.11 Adhesion testing

Simple adhesion testing was performed on a range of substrates and film combinations using a combination of scotch tape, double sided polyimide tape and PDMS. Results such as completeness of removal and film defects were recorded roughly by photographs and notes, and have already been mostly reported in Chapter 3.8.

3.12 Field-effect scanning electron microscopy

To corroborate AFM scans of metal films, a FEI Co. APREO™ FE-SEM was used to image the surface of 100 nm thick Au films sputter coated at 0.95 Å s^{-1} on PMMA sheets for model system FDTR I. Two pieces of copper tape were placed carefully

on the Au surface and attached to the metal sample holder to create a conductive pathway with a 1.5 mm spacing in which to view the sample. Samples were imaged in immersion mode using SE and BSE detectors at voltages of 2-5 kV and magnification up to 350 000x with emission current and image averaging adjusted to yield optimal contrast.

4

Results

This chapter begins with a look at literature spin curves and results from the step edge fabrication method developed herein. Properties of spincoated polymer films are then investigated in the following order: thickness, roughness, defects, internal structure and chain alignment. Metal films are subsequently investigated, with comparisons to previously presented work [1]. Lastly, initial results from the PVA-based water soluble release layer are presented.

4.1 Towards spincoating thickness

Suggestions from literature spin curves

To determine initial concentrations and relevant spincoating models, it is useful to look at literature examples. Yun et al. spun $\overline{M}_w$ 93 000 PMMA from anisole solutions of 4.8 to 20.0 wt.% at speeds 2000 to 5000 rpm [71]. Data from Figure 2 of [71] is reproduced in Figure 4.1 and plotted against both spin speed and concentration. For these data, (2.12) yields the better fit with R^2 values of 0.993 compared to 0.937 for (2.13). This is in contrast to the results of Tippo et al. [27]. Values of A, n and α are then readily determined to respectively 330 $\pm$ 290, 1.83 $\pm$ 0.05 and 0.45 $\pm$ 0.17. If the theory was consistent, it would have been sufficient to make one spin coated film at known c and ω to find A for solutions of each $\overline{M}_w$ used herein. Clearly, variations in n with changing ω are very low, while the values for A and α vary a lot with changing c, it will therefore be necessary to make spin curves for each

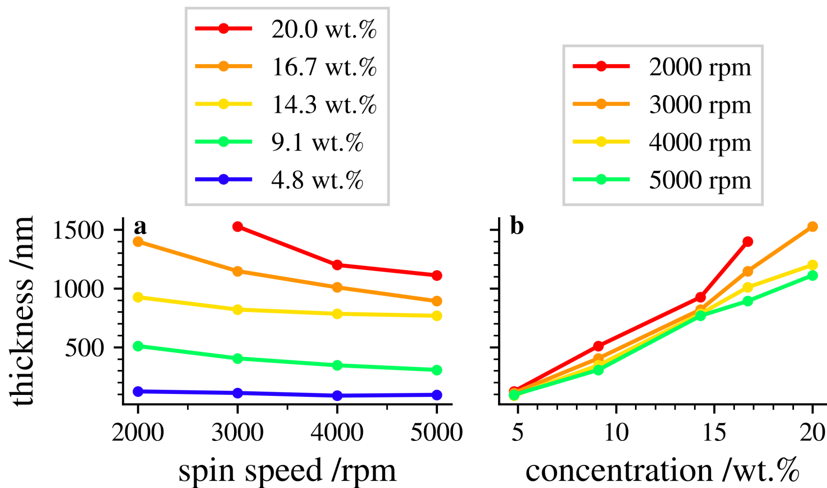

Figure 4.1. Literature spin curves from PMMA of $\overline{M}_w$ 93 000 in anisole plotted against spin speed (**a**) and concentration (**b**). Data were reproduced from Figure 2 of [71].

concentration. For concentrations of about 5 wt.% and lower, it is clear that variations in thickness with spin speed are low compared to the uncertainty of measurement, thus changing polymer concentration should be used to alter thickness of such films, keeping the spin speed constant.

Thickness by vertical scanning interferometry

Results from fabrication of step edges showed that the quality of the step and the surface was imperative for repeatable thickness measurements. The step edge shown in Figure 4.2a indicates such a surface before tilt removal, where the horizontal shift in colors indicates the unfiltered difference in light travel time. To create such a smooth step using the method outlined in Chapter 3.3, samples must be pressed hard onto the double sided tape. In the case of insufficient adhesion forces, the weight of the glass slides will push on the samples, in some cases shifting the solvent line gradually upwards. In severe cases, the solvent contacts the tape, generally causing detachment and subsequent loss of all films.

Filling the beaker with minimized shaking, after placing the samples was also deemed important for an even solvent line. For films thinner than 2 µm, the optimal immersion time was about 5 min, to allow complete film removal, while also avoiding the polymer bead that would form on the step at immersion times of 10 min. For very

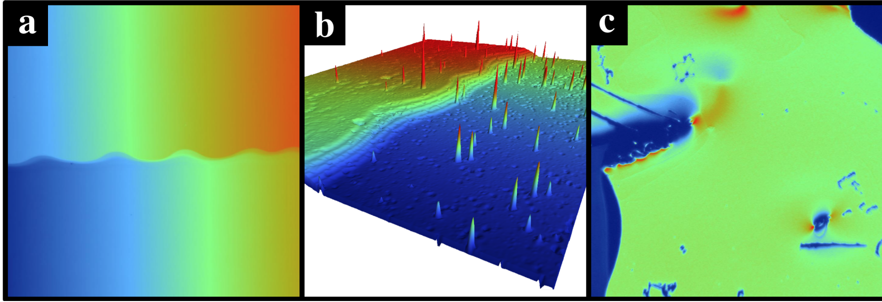

Figure 4.2. **a**, raw height data of a smooth step edge on a smooth surface. **b**, 3D rendering of step edge created on a rough 500 nm e-beam deposited Au substrate. Colors range $\sim$1 µm from blue to red. **c**, image of Au surface seen in Figure 3.3e as peeled from an Si substrate by partly melted PMMA. Colors indicates arbitrary intensity of greyscale image from blue to red.

rough films, such as the one imaged in Figure 4.2b, or for step edges with a high amount of defects, film thickness could not be determined and the stylus profilometer was used as an alternative. From a dataset of 12 different samples ranging from 170 to 2700 nm, the optical profiler reports, on average, heights 9 % above than the stylus profilometer.

4.2 Polymer film thickness for FDTR II and 3ω model systems

Having proved the repeatability of the developed methods, test samples could be fabricated. Spin curves from polymer concentrations ranging from 1 to 10 wt.% at two different polymer $\overline{M}_w$ and multiple spin speeds are given in Figure 4.3. The expected behaviour of non-linear increase in thickness with c and decrease in thickness with ω can be observed. For fabrication of 3ω samples of thickness range 400 to 1000 nm, it is clear that the 10 wt.% solution of $\overline{M}_w$ 750k is too thick, while both those of $\overline{M}_w$ 120k 10 wt.% and $\overline{M}_w$ 750k 5 wt.% would satisfy the thickness requirements. The 5 wt.% solution of 750k PMMA was chosen to allow experiments with FDTR models I, II and 3ω models to correlate better. The point at 510 nm and 2000 rpm, indicates a total range of 800 to 250 nm for spin speeds of 800 to 8000 rpm as given by $L_1 = L_2\left(\omega_1/\omega_2\right)^{-\alpha}$ from (2.9), assuming $\alpha = 0.5$.

Spin curves from Si calibration chips and sample thickness for 3ω samples are given in Figure 4.4. A least square fit to (2.9) was performed and spin speeds were

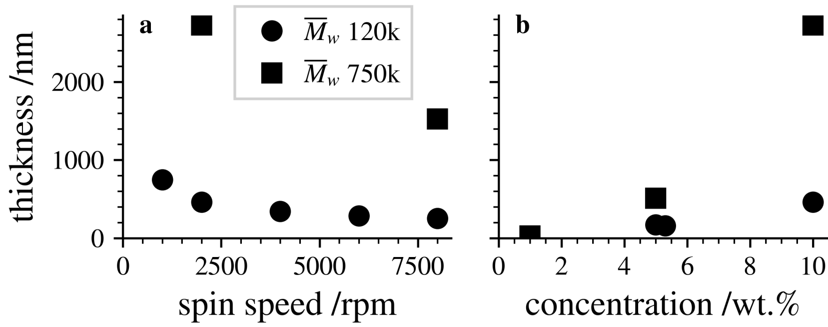

Figure 4.3. **a**, spin curves from two different $\overline{M}_w$ of 10 wt.% PMMA in anisole. **b**, thickness variation by concentration from spinning at 2000 rpm for two different $\overline{M}_w$.

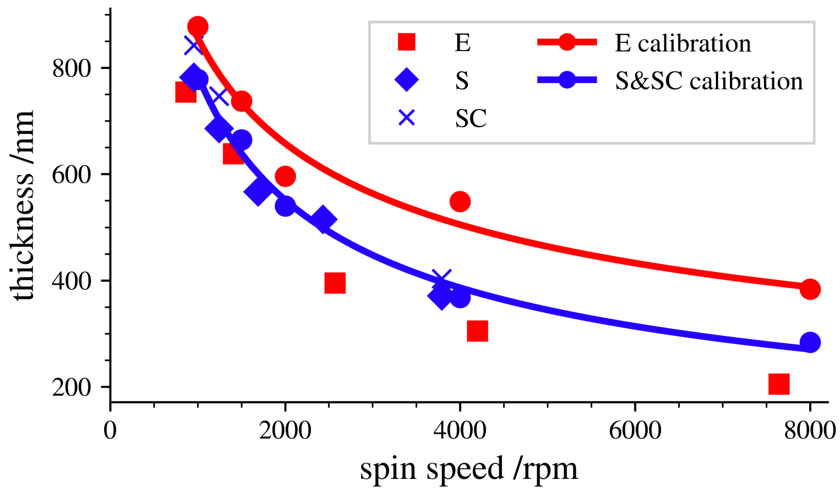

Figure 4.4. Reference spin curves on Si substrates produced before sample fabrication (circles) compared to actual thicknesses achieved (diamonds) on 3-omega samples of type S, SC and E. All thicknesses were measured by the optical profiler, except those of samples of type E which were found by the stylus profilometer. Solid lines are best fit to the respective reference spin curves. Two samples of type SC were lost during step edge fabrication, explaining the lack of datapoint.

calculated from (2.10). E-beam deposited metal proved to be extremely rough as seen from Figure 4.2b, thus estimation of polymer thickness was performed by hand from stylus profilometer curves similar to those seen in Figure 3.2b. Figure 4.4

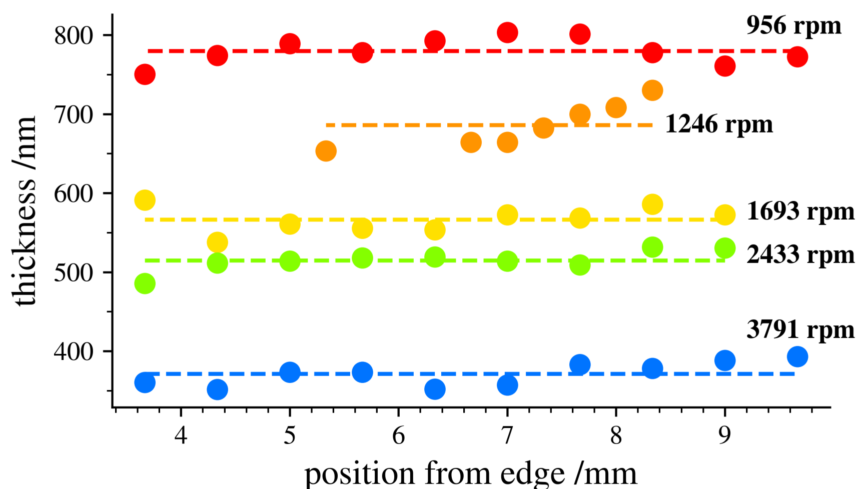

Figure 4.5. PMMA film thickness measured by the optical profiler in a straight line from the sample edge for each thickness of sputtered Au 3ω samples without carbon (samples of type S). Dotted lines indicate mean height.

indicates that there is no consistent change when going from an Si substrate to a Au substrate. The rougher e-beam deposited film seems to consistently form films up to 50 % thinner than what was expected from the Si test.

Thickness uniformity is especially interesting for measurement of thermal properties, and so Figure 4.5 gives thickness changes as measured by the optical profiler along a set of step edges for as-fabricated 3ω samples of type S. Mean peak-to-peak difference is 9.11 % and the uncertainty for each thickness is 3.3 %. A slight trend of increasing thickness towards the center of the samples (right side of figure) is also seen, indicating a slight systematic unevenness in the polymer films. Note that the 1246 rpm sample had an uneven metal film, likely explaining the increased height variation.

Thickness by AFM

No polymer film thinner than 130 nm could be accurately determined by either VXI or the stylus profilometer. Such films were more effectively measured by AFM using a soft cantilever on step edges created by scraping polymer with a sharp cocktail stick as steps created by immersion in solvent exceeded the 13 µm maximum scan length. A stiff (40 N/m) cantilever in PeakForce mode did not notice the abrupt change

in height. FTIR II polymer films were successfully measured with the following results: The Si-PMMA-4000 rpm sample was measured on five different points to (22.5 ± 0.6) nm, with only 1.5 nm increase from the center and out. The Si-PMMA-8000 rpm sample was measured on two different points to an unexpected higher mean of 26.0 nm. This sample was also the roughest of the two, indicating how spin speed is less important compared to handling in this thickness range.

4.3 Surface and interface roughness

Roughness by phase scanning interferometry

Roughness of Si and Au covered substrates was readily captured by PSI and found to be nominal around 1.5 nm with $R_q = S_q$, indicating random rough surfaces. The roughness of Au substrates from samples of type S was compared by both PSI and AFM and found to be very similar as seen from Figures 4.6 and 4.7, with the PSI yielding slightly higher values. Roughness of metal could not be measured accurately after PMMA coating due to contamination and defects introduced in the process as presented in Chapter 4.4. Characterization of PMMA-Au interfaces also failed in the cases of model systems FDTR I and III. The 1.1 cm thick PMMA sheet attenuated too much light to yield a usable signal and the melted polymer had a rough surface that scattered all light. The interface side of an Au film could, however, be measured by AFM after peeling as presented in Chapter 4.7.

PMMA roughness by atomic force microscopy

As the optical profiler has limited lateral resolution, and the polymer film is transparent, AFM presents itself as the desired tool for detailed surface mapping. As seen from Figure 4.6, polymer films are significantly flatter than their respective substrates, without large film-to-film deviations. The AFM is able to capture smaller contamination and pin-hole defects as seen in the insert of Figure 4.6, but quantification is challenging and time-consuming at scan areas of only $(10 \times 10)\,\mu m^2$. PMMA slabs were found to be smooth, albeit with surface cracks as thoroughly discussed in [1].

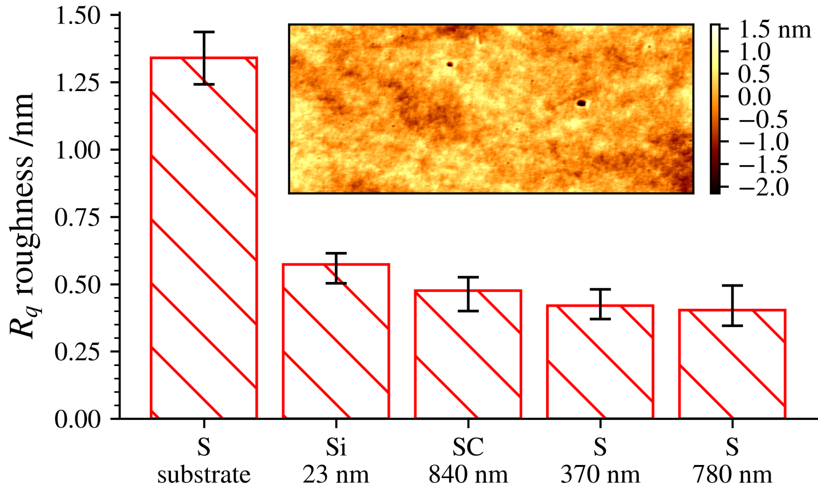

Figure 4.6. Mean R_q roughness as measured by AFM for substrate and PMMA films averaged over 3-5 maps. Error bars indicate maximum and minimum. Bar labels indicate the substrate or 3ω sample followed by mean PMMA thickness. Insert displays a height map of the *S-780 nm* sample as captured by AFM. The long axis of this map is 2 µm.

4.4 Defects quantification

Polymer thin films produced by spincoating are prone to defects as explained in Chapter 2.4. Metal films are generally less prone to defects due to the controlled environment in which they are fabricated. Later processing steps or poor handling may, however, cause contamination, unwanted roughness, cracks or other defects in in both polymer and metal films. Quantification of such defects is important to optimize fabrication parameters such as cleaning steps, spinning parameters and handling precautions. Defect quantification may also be useful to verify the integrity of each sample once the process is optimized. The development of such a method was therefore endeavoured as part of this thesis work using the newly acquired Contour GT-K optical profiler and the Multimode AFM.

Roughness by phase scanning interferometry

Despite its superior resolution, the used AFM offers severely limited scan sizes and data acquisision speeds. The optical profiler can gather data from a large portion of the sample area in a matter of minutes. Considering each sample to have an area of

100 mm^2, the fraction of area scanned in 16 maps of (323×431) µm^2 is minimum 2.2 %, which should be acceptable to characterize defects. It is important to note that only the difference in roughness between film and substrate bears any meaning in the optical profiler data, for as realized by comparing Figures 4.6 and 4.7, the optical profiler observes the substrate through the film, while only AFM measures the actual surface roughness. It is clear from the inserts that samples of type E are very rough as was also indicated by its opaque appearance visible to the naked eye. Contrary to what should have been the case for defect-free transparent films, spincoating PMMA generally seems to increase roughness by up to 3 times, with the thickest samples presenting the roughest surface. All samples were also visually covered with Si particles from dicing, which may partly explain the increased roughness values. Separating film defects from contamination is not possible as contamination present before spincoating may cause defects.

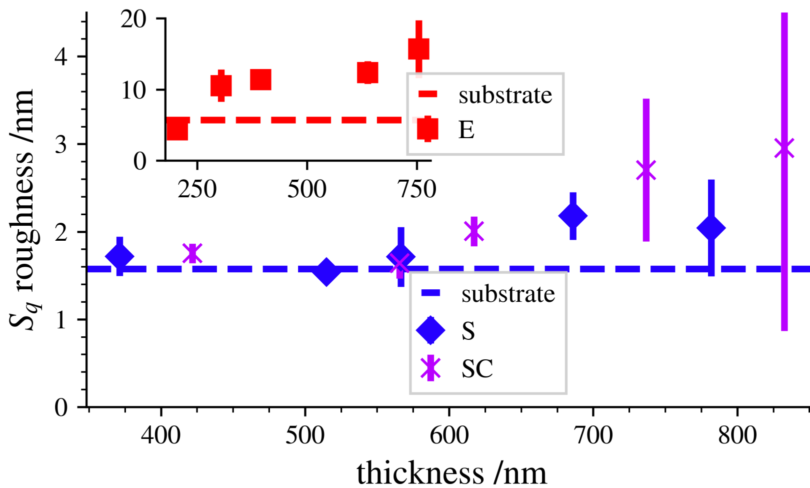

Figure 4.7. S_q roughness measured by the optical profiler of 3ω samples of type S, SC and E as a function of PMMA thickness. Error bars indicate standard deviation. The difference in polymer and substrate roughness indicates actual roughness added by the polymer spincoating.

Samples of type S and SC have, in accordance with their relatively smooth substrate, lower roughness than samples of type E. Also here, a general increase with increasing thickness is observed. The two thickest samples of type SC had visually uneven metal coatings, which may contribute to the higher roughness and the large standard deviation.

As the interpretation of S_q is not always straight-forward, a more direct parameter would be the total displaced volume of the defects and contamination. The total displaced volume from the same data as in Figure 4.7 is presented in Figure 4.8. It is clear that the trends align with those of Figure 4.7, albeit with larger relative changes. The mask defining abnormally high or low pixels was ineffective in isolating contamination and film defects from substrate features for samples of type E, causing the very large reported volumes.

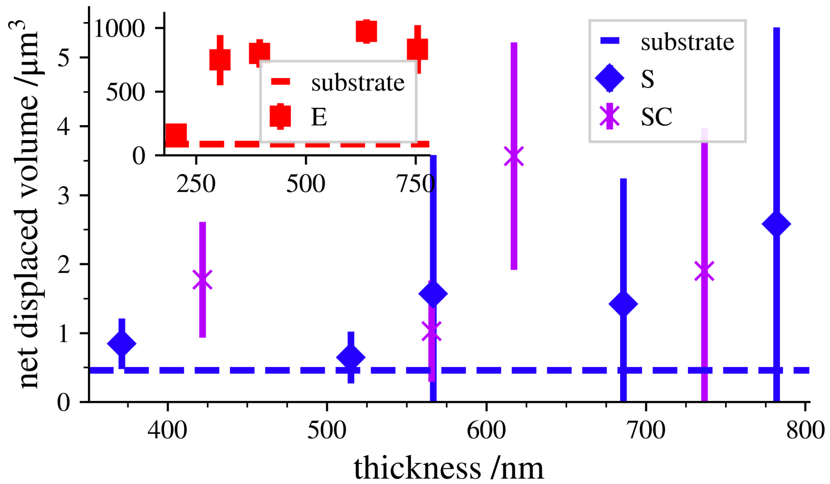

Figure 4.8. Net displaced volume as calculated by Vision64™ software from masked surface data of 3ω samples of type S, SC and E. The SC sample with the thickest film was fractured and therefore removed from the data.

Metal film defects of peeled FDTR III model system samples

Melted PMMA was sufficiently adherent to peel uniform Au films as seen in Figure 3.3e. Inspection in the optical profiler proved the peeled Au surface to be largely homogeneous with some defects in places of incomplete melting as seen in Figure 4.2c. Areas with fully melted PMMA appear to be very smooth and polymer-Au adhesion was superior to that of tape-Au as revealed by a simple scotch-tape test.

4.5 Polymer bulk structure by μ-Raman spectroscopy

From Figure 4.9a and c, highest PMMA peaks are seen at 600, 810, 967, 987, 1450 and 1720 cm^{-1}. The spectra of Si and SiO_2 substrates are included for reference and

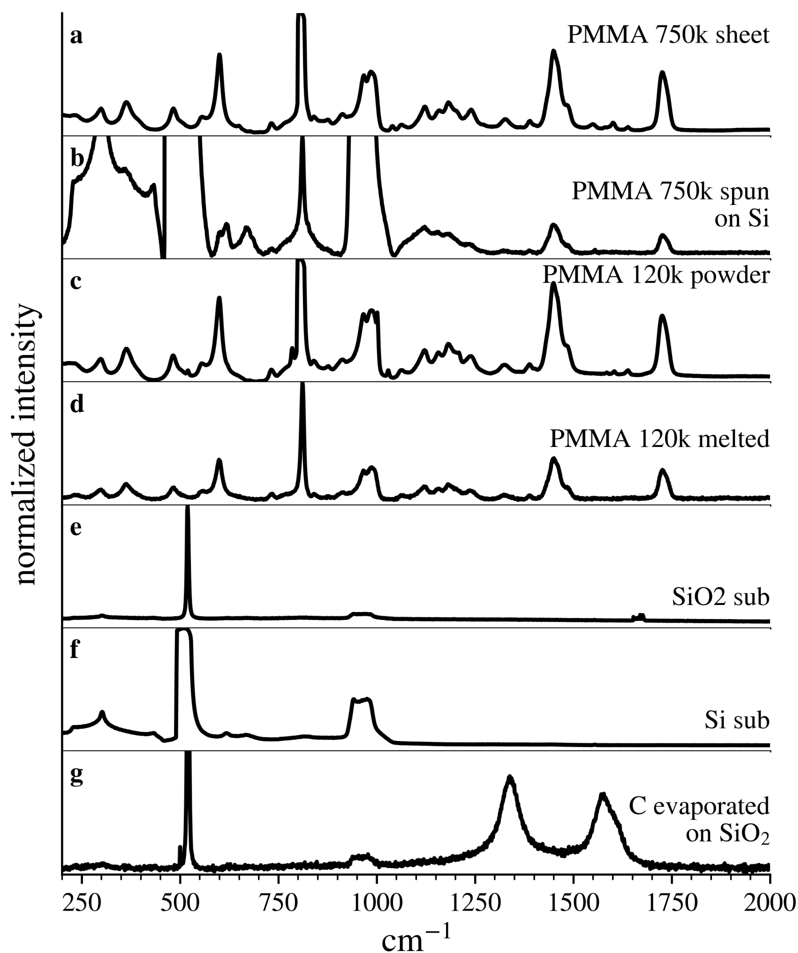

Figure 4.9. **a**-**f**, μ-Raman spectra of PMMA in different forms and of different substrates. PMMA spectra (**a**-**d**) are normalized to the 810 cm^{-1} peak, while remaining spectra are normalized to the highest appearing peak. Baseline subtraction have been performed on spectra **b** and **d**. **g**, μ-Raman spectrum of evaporated carbon.

demonstrates that the PMMA peaks at 810, 1450 and 1720 cm^{-1} are best separated from the substrate peaks. 810 to 1720 cm^{-1} range is also within the system-specific 1231 cm^{-1} range of a more rapid narrow shift scan that allows spectra of even 20 nm PMMA films to be captured with good signal-to-noise ratio in as little as 5 min on the Renishaw spectrometer. PMMA of $\overline{M}_w$ 750k and 120k seem to be largely similar. Both spun and melt cast PMMA differ in that the 810 cm^{-1} peak has gained intensity relative to the other peaks. Comparing spectra from spuncast PMMA to that of the PMMA sheet is simplified by removing the large flat Si background at lower shifts. Clearly, peaks from spuncast PMMA are harder to separate from the background noise due to the reduced amount of material, but all peaks are still visible, having the same form and at the same shift. This similarity indicates little change in polymer internal structure through dissolving in anisole and subsequent spincoating.

Figure 4.9g is included to verify successful carbon deposition and allude to the allotrope of the deposited material. The spectrum was acquired from one of many dark spots, 1 µm or smaller, scattered over the surface of the SiO_2 reference sample. Similar spectra were obtained from a map scan of the surface, indicating the omnipresence of carbon, although not visible in the microscope.

Spectra of PMMA films of different thickness treated identically to fabricated

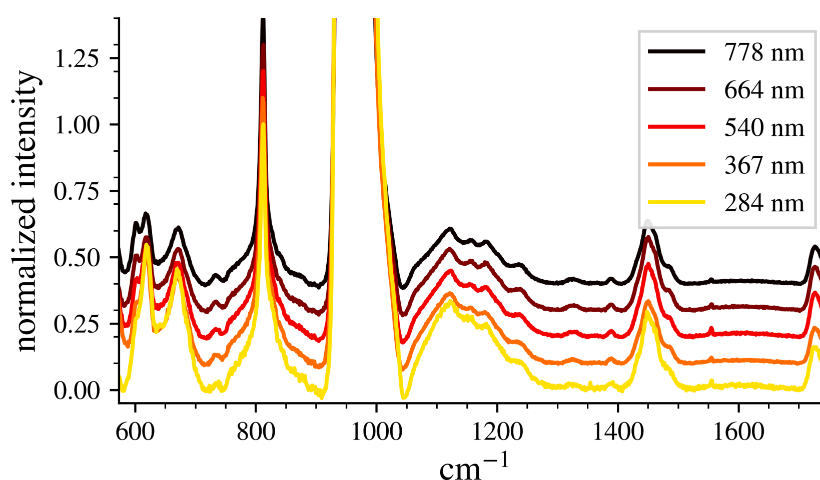

Figure 4.10. µ-Raman spectra of films of different thickness spun from the same solution on Si substrates. All spectra are normalized to the PMMA peak at 810 cm^{-1} and substrate baseline was subtracted.

3ω samples, but on Si substrates are shown in Figure 4.10. The spectra indicate no change with different thicknesses apart from the expected decrease in signal-to-noise ratio, which is directly dependent on the amount of sample in the interaction volume.

4.6 Polymer molecular chain alignment

Figure 4.11 shows intensity of polarized µ-Raman spectra acquired with polarization parallel and perpendicular to the radial direction for three different polymer films. The uppermost two spectra were captured using a pinhole to reduce the substrate signal. The two 5 wt.% films show no difference between the two orientations, while the 10 wt.% films demonstrate a clearly higher PMMA intensity when beam polarization is oriented parallel to the radial direction. Contrary to the films from 5 wt.%, the film from 10 wt.% solution was not annealed to avoid any potential reorientation of the polymer. No difference in polarization was observed for an identical, but annealed PMMA film, nor for any of the tested films spun from 5 wt.% solutions. Thinner films were not investigated for polarization effects.

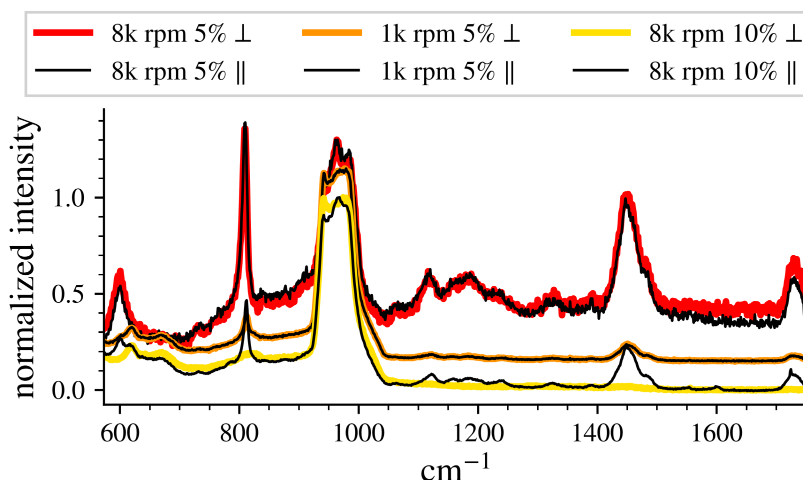

Figure 4.11. µ-Raman spectra with light polarized perpendicular to (thick) and parallel to (thin) the radial direction for three different samples. The labels refer to the speed of spinning and the wt.% concentration of $\overline{M}_w$ 750k PMMA - anisole solution resulting in ~400 to 1500 nm films. All spectra are normalized to the highest peak and shifted vertically for clarity.

4.7 Metal growth

Thickness of metal films was attempted verified by the optical profiler, however, either rough edges or high difference in reflectivity caused poor data quality. Only the thickest metal films yielded usable data, and those were very rough, yielding (410 ± 40) nm thickness from a total of 8 scan areas. Hence, nominal thickness of 500 nm as calculated from QCM-calibrated deposition rate and deposition time will be trusted. The AJA has calibrated coating uniformity of 0.5 % on 4 in wafers, therefore, metal films are expected to have equal thickness across the entire substrate.

Knowledge of the internal structure of metal films used in TBC measurements is crucial, especially when comparing experiment and simulation. A large set of high resolution AFM scans of metal films of different metals, thickness and on different substrates has been gathered in the course of this research and a choice subset can be studied in Figure 4.12. As the images were captured in PeakForce mode, the system is more sensitive to changes in material properties than height. Deformation maps were therefore chosen as they provide the best contrast for the surface features in question. It should be noted that trenches appearing in Figure 4.12c and e are features of the PMMA substrate, not the metal films.

Detailed comparisons of these maps would be superfluous due to the varying metals and substrates. It can, however, be observed through Figure 4.12a, b, c, f and g that there is a general trend towards features of larger lateral size with increased thickness. There are also no abrupt changes between different substrates and metals indicating similar growth modes. Repeated attempts of computer quantification of feature size have proven fruitless, thus the general observation remains that the rate of growth seems to slow as the films grow thicker in loose accordance with (2.14). The height of these features is in the 1-4 nm range with a slight tendency towards increasing height with increasing film thickness although not as pronounced as the increasing lateral size.

Double sided comparison by AFM

For FDTR samples, the metal side facing the polymer is also highly interesting. Low adhesion between metal and polymer film is detrimental for TBC, but allows peeling of the metal film to compare the two sides as described in Chapter 3.4, and resulting height maps are presented in Figure 4.13a and b. Figure 4.13c reveals how the Au film was severely buckled by the peeling process. Scanning on a relatively

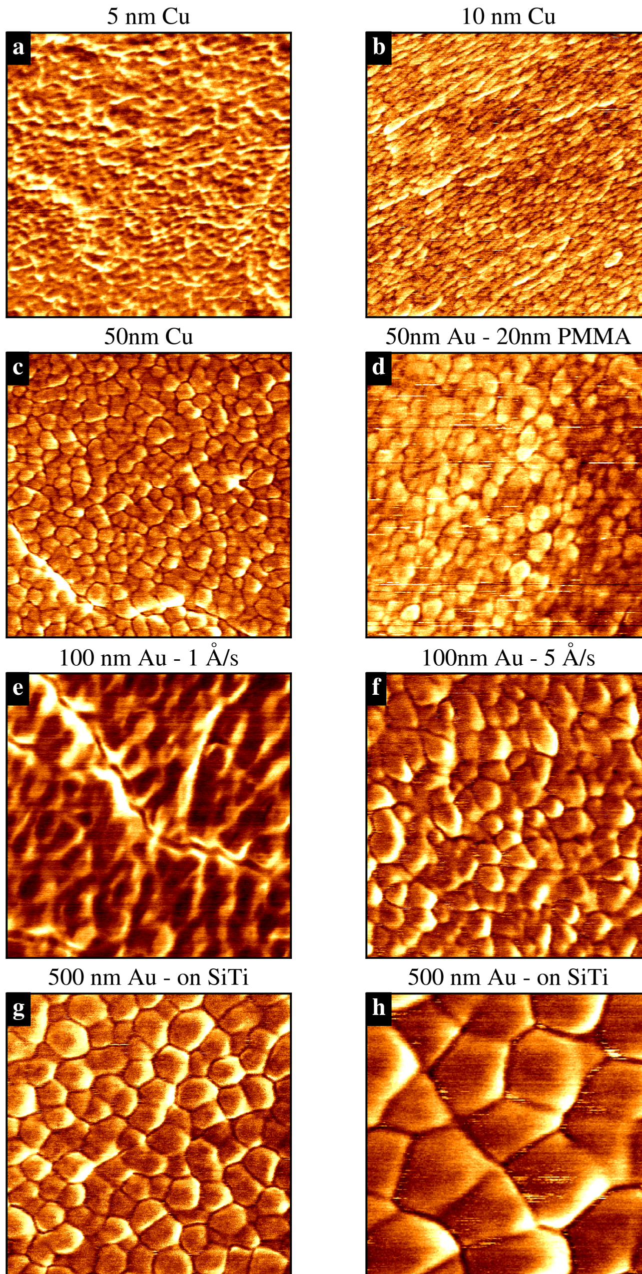

Figure 4.12. AFM deformation maps of metal films of different thickness captured with RTESPA 40 N/m probe. Films **a**-**f** are deposited on PMMA sheets, while the figure text indicates substrates for the remaining samples. **a**-**g**, $(500 \times 500)\,\mathrm{nm}^2$. **h**, $(200 \times 200)\,\mathrm{nm}^2$.

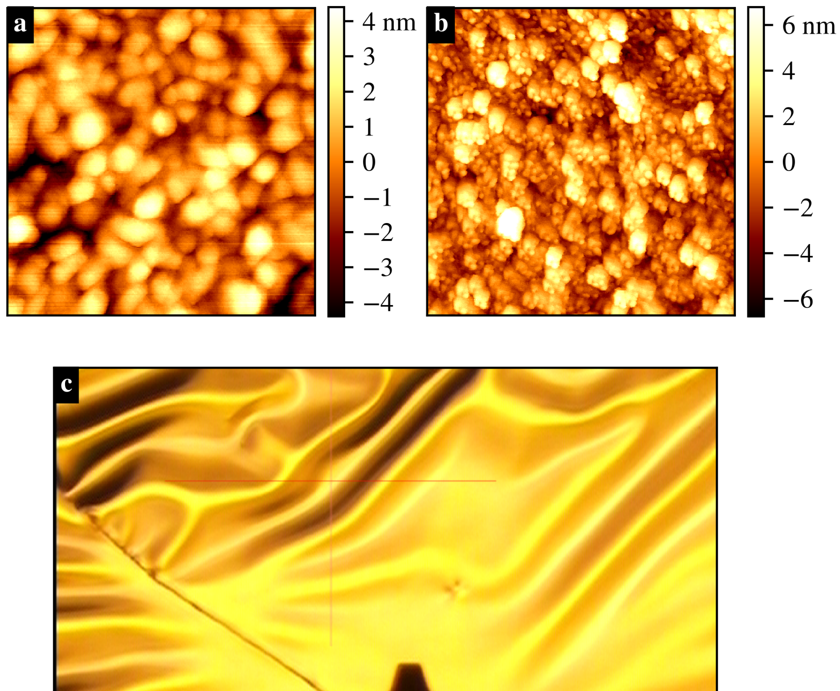

Figure 4.13. AFM height maps of surface side (**a**) and PMMA-facing interface side (**b**) of a 100 nm Au film peeled from a PMMA sheet. Both maps are (500 × 500) nm^2 captured with SA-AIR 0.4 N/m probe. **c**, bright field microscope image of the buckled Au film, unspecified scale. The trapezoid dark spot in the bottom center of the image is the cantilever tip indicating the scanning location, unspecified scale.

flat surface was endeavoured to minimize the effect of this buckling on observed features.

The interface side has a fractal-like structure of continuously smaller features down to ∼5 nm. Smaller features appear to be located on top of the larger features, predominantly on the bottom side. The surface side has, as also observed in Figure 4.12, regularly sized features of ∼30 nm. From the height scale it is clear that the space separating features is also clearly deeper on the interface side, indicating an interface rougher than the surface. R_q values for four (500 × 500) nm^2 maps were 2.6 and 1.4 nm for the interface and the surface sides, respectively, verifying that the interface side is indeed rougher on this length scale.

FE-SEM on metal films

Figure 4.14 compares AFM and FE-SEM images of the same 100 nm Au on PMMA sheet sample discussed above. As the sample is extremely flat the BSE image is chosen for FE-SEM and the deformation map is chosen as the PF-QNM map to obtain optimal contrast. Both maps were captured close to the center of the sample. The BSE image indicates more features than visible the QNM map, hinting at the presence of metal density changes buried beneath the topmost layer.

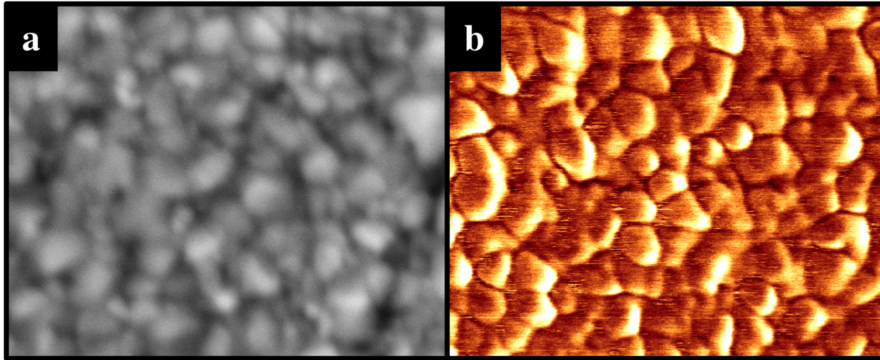

Figure 4.14. Comparison of FE-SEM backscattered electron image captured at 5 kV and 100 pA (**a**) and PF-QNM deformation map captured with RTESPA 40 N/m probe (**b**). The width of both images are identical and equal to 500 nm.

4.8 Novel water soluble release layer for QSTF model fabrication

Dissolving PVA to 5, 10, 15 and 20 wt.% in deionized water solution was achieved, yielding films of up to ~7 µm after spinning as described in Chapter 3.9. Dissolving to 30 wt.% was not achieved and even at 20 wt.%, the solution gelled after some weeks of storage. 5 wt.% PVA solution did not yield homogeneous films on bare Si substrates.

Dried PVA films proved to be chemically resistant to both anisole and acetone, and spincoating of PMMA thin films from both 1 and 8 wt.% solutions was readily achieved. After leaving three Si/PVA/PDMS stacks in water overnight as seen for one sample in Figure 4.15a, PVA had gone from solid to gel, releasing all Si chips and leaving the PMMA film from 8 wt.% solution on the PDMS. This film could subsequently be partly transferred to a Au coated wafer seen as the very cracked surface in Figure 4.15b. Spincoating of PMMA from 1 wt.% solution did not appear to be successful as no trace of this film was observed on the PDMS slab.

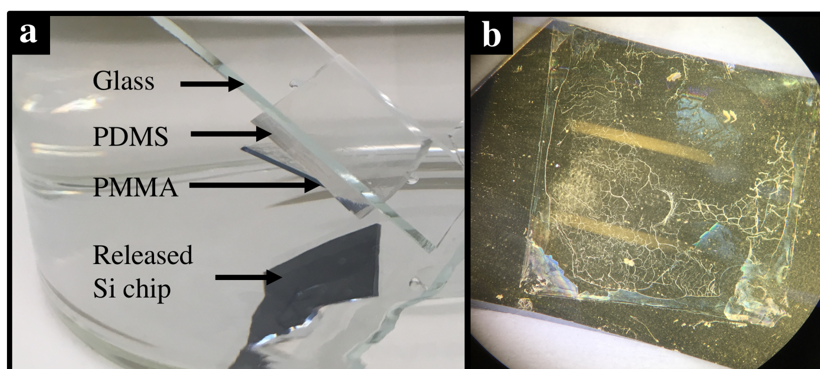

Figure 4.15. **a**, glass-PDMS-PMMA-PVA-Si stack after Si substrates are released to the beaker bottom by the dissolving PVA. **b**, attempt at transfer printing of the PMMA film from **a** to a Au-covered substrate. PDMS folding afforded several cracks in the rigid PMMA film. Poor image quality affords reflections from the surroundings to be visible.

5
Discussion

The discussion follows the results section closely with thickness, roughness and μ-Raman spectroscopy results for polymer films being discussed before metal structure, carbon interface layer and water soluble release layer. Focus is given to usability of the different tools with regards to speed of data acquisition, reportability, degree of invasiveness and accuracy. Lastly follows a brief discussion of interface property measurements that can be improved in future investigations.

5.1 Step height fabrication

Partly immersing polymer-film covered substrates in solvent proved to be a simple and rapid method for fabricating step edges. However, an improvement in repeatability and in speed could likely have been achieved by the use of a computer-controlled dip-coating apparatus. Though still continuing the extra step of attaching samples to a glass slide, this method allows the controlled immersion and withdrawal from the solvent bath.

5.2 Thickness measurement

Thickness measurements for films in the 130-2000 nm range obtained using VXI proved to be both rapid and repeatable with thickness variation on the scale of instrument uncertainty. As 3ω heater lines are typically 2 to 3 mm long, isolating the data to those in the center of each sample yields mean thickness variation 2.0 %,

which is acceptable [22]. The optical profiler is fast and accurate, but the step edge is a destructive method for measuring thickness. Clearly, the use of an equally fast and accurate technique over the whole area of the sample would have been optimal to yield accurate knowledge of sample thickness variations.

The 9 % difference in measured thickness between stylus and optical profiler is quite high when compared to the 3.3 % uncertainty of 1 cm^2 samples as seen from Figure 4.5. This difference can be partly attributed to four points:

- The stylus profilometer only scans one line per point of thickness, while every thickness measurement from the optical profiler is an average over a 0.14 mm^2 area.
- Optical profiler height values were read manually from data plots, which were complicated by the difference in apparent tilt between film and substrate.
- The stylus tip of radius 6.5 µm set to force 30 mN may have indented the polymer film.
- The stylus profilometer was recently calibrated, but had not received maintenance for some time, while the optical profiler was newly acquired.

In light of these problems, this stylus profilometer should not be pursued to measure step edge thickness.

The AFM is able to capture thickness reliably, but this method also suffers from being invasive and especially from being slow. The height uncertainty of 2.7 % is comparable to that obtained using VXI for thicker polymer films. In the force-controlled mode preferred for the Multimode AFM, a stiff cantilever is not able to respond to the the sudden change in material properties from Si to PMMA on the step egde. If PMMA is replaced for a softer polymer in the future, sample indentation causing erroneous thickness readings may also be a problem with the softer cantilever, as already observed in the case of a 40 N/m cantilever on 20 nm PMMA.

Neither AFM nor VXI are optimal tools for thickness measurements of samples studied herein, one being slow and both being invasive methods. Clearly, in-situ thickness comparisons during FDTR measurements would be ideal, using for example picosecond acoustics as done for multiple Si/polymer/metal stacks in [12]. However, the current FDTR setup does not have a delay stage, thus this option is unavailable. Ellipsometry is a common, non-invasive method for measuring coating thickness in the entire thickness regime probed in this thesis work [72]. Lateral resolution is, however, limited for most instrumental setups to the millimeter range. For FDTR measurements, where the beam size is in the micron range, film thickness has to be known accurately, so a method with high lateral and vertical resolution

would still be used to verify the uniformity of film thickness in addition to averaged measurements by ellipsometry. Upon rapid iteration through system parameters, mechanical and optical properties of new interface films or structures may pose challenges to established thickness measurement routines, which should be considered when designing interface modifications.

5.3 Spincoating of polymer films

Results from spincoating 750k PMMA - 5 wt.% indicates no consistent change when going from Si to Au-coated substrates. Thus, spin curves based on Si substrates seem to be a valid and rapid method to find spin speeds for evenly distributed thicknesses in the target range 400 to 1000 nm. Furthermore, polymer films spun on Si should be identical to films spun on Au in internal structure as any significant differences caused by the spinning process should have been manifested as different thicknesses. Thus, films on Si and SiO_2 probed by µ-Raman spectroscopy can be used to describe identical films on Au substrates, which are not accessible to Raman characterization.

Thickness has been measured for only two PMMA thin films from 750k PMMA in 1 wt.% solution, however, multiple films have been spun successfully from solutions of viscosity down to 120k PMMA - 0.8 wt.%. Concentration is a more accurate method for controlling thickness as described in Chapter 4.1, thus precise thickness variation in the lower concentration regime should not be an issue, only lacking a confirmed protocol to produce defect-free films.

5.4 Sample roughness and defect quantification

PMMA roughness by atomic force microscopy

Film roughness by PF-QNM appears to be largely consistent over the different polymer films investigated herein. No consistent increase of roughness with polymer film thickness indicates that the same low roughness is expected for all PMMA films spuncast on smooth substrates. As mentioned, the height differences may be underestimated when using hard cantilevers, adding to the uncertainty of the absolute value of these roughness data. The relative values should, however, not be affected for samples of the same material, and the absence of significant polymer roughness was confirmed by the optical profiler. The quantification of widely spread defects is also problematic. The two valleys seen in the insert of Figure 4.6 are clearly not

uniformly distributed on this length scale, thus a larger scan area than $(10 \times 10)\,\mu m^2$ is needed to see systematic defects and should be pursued for example by using the other scanner capable of capturing $(150 \times 150)\,\mu m^2$ maps, albeit with lower lateral resolution. Film defects are most crucial for QSTF samples as polymer films are thin, and contact between the two metals may lead to a conductive pathway, ruining the sample with respect to obtaining a measurable TBC.

E-beam evaporated film roughness and coverage

Au films deposited by e-beam evaporation (3ω samples of type E) proved to be exceptionally rough, with roughness values hardly comparable to those of other substrates or metal films produced herein. Based on the growth theory of Chapter 2.4, this may be attributed to low adatom kinetic energy resulting in non-equilibrium growth and large shadowing effects. Thick metal films should either be deposited using sputter coating or at elevated substrate temperatures to improve the metal structure. Thickness measurements performed by stylus profilometry are only indicative, however, the polymer does not appear to completely cover the substrate as indicated by the µm roughness seen in Figure 3.2b, rendering these samples useless for 3ω measurements. Variations in both roughness and total displaced volume can potentially be attributed to differences in how the polymer film fills the voids and coats the peaks of the metal film. Such an investigation would, however be of purely theoretical interest as the Au film has already been discarded as too rough, thus data from samples with evaporated Au films will be disregarded in the remainder of this thesis.

Phase scanning interferometry for defect quantification

PSI measurements were performed to obtain a quantitative estimation of defects of PMMA films and contamination incurred during fabrication. S_q is not very well suited for characterizing these types of defects as it is a parameter used to describe surfaces of uniform height distribution making it hard to quantify sensitivity to different types of defects. Therefore, net displaced volume will be the focus of the following discussion. The initial assumption was that a larger volume of PMMA should be able to accommodate more internal stresses and be less prone to defects compared to the thinner PMMA films which could more readily delaminate or contract, creating cracks and pinholes. Contrary to initial assumptions, net displaced volume plots show increasing volumes with increasing film thickness.

Positive correlation between defects and thickness may be explained by factors

of the experimental setup. As the PMMA film is transparent to the optical profiler, a valley in the polymer will appear as a peak and a particle resting on top of the polymer will appear to be far removed from the substrate surface as seen in Figure 5.1f and a respectively. As PMMA thickness increases, equally wide valleys will appear as higher peaks and contamination will appear further removed from the substrate. Data processing performed by the software makes it hard to quantify this effect and correct for the change with thickness as steep slopes may exceed the stated 72 square degree (deg^2) slope limit of the optical profiler. Indeed, a brief inspection of Figure 5.1 demonstrates how the main component of the total displaced volume should be positive as the peak in e is not expected to occur. The data reveal, however, that the negative component of the displaced volume is five times higher than the positive component, an observation that has yet to be explained.

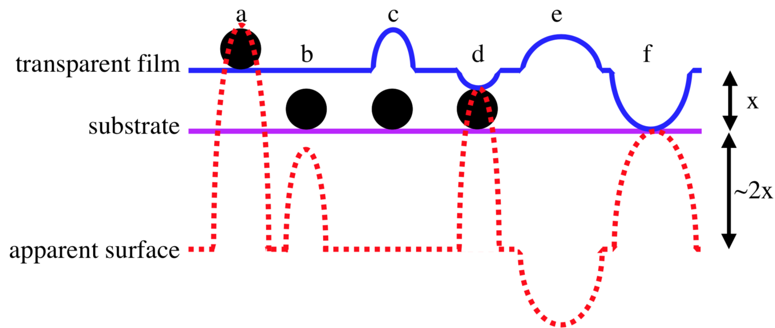

Figure 5.1. Illustration of how defects (black disks) on various locations should affect apparent surface profile as measured by VXI. Examples are given for a polymer resting on top of (**a**) and beneath (**b,c,d**) a transparent film, with (**c,d**) and without (**a,b**) affecting the polymer film morphology. **e** and **f** are an example of polymer peak and pin-hole, respectively.

Using roughness and total displaced volume data to compare defects and contamination of samples with films of identical thickness or substrates with thin or no transparent coatings can still be assumed to be valid. Hence, PSI is a valuable tool for process optimization. The higher displaced volume for most samples of type SC compared to those of type S is illustrative of such a comparison as the samples of type SC were exposed to a dirtier environment during carbon coating and the carbon coating is known to be inhomogeneous.

To fully utilize the power of the technique, VSI should be replaced by VXI for better compensation in the case of large defects or contaminant particles, and stitched greyscale images of the entire sample surface should also be captured. The captured

images should be used to identify the type of defects, similar to what a regular optical microscope could afford, but faster. Combining VXI with imaging should yield better quantification and reportability than either technique alone.

5.5 µ-Raman spectroscopy of PMMA

When fabricating polymer films in a range of thicknesses to find TBC as a series conductance by extrapolating to zero thickness as for 3ω and QSTF measurements, it is important to know that polymer conductivity and heat capacity remains identical for all thicknesses. Polymer alignment as a result of high solution viscosity and substrate interaction during spincoating can result in alignment of macromolecules, altering PMMA properties from isotropic to anisotropic.

A PMMA thin film was spun from 750k PMMA - 10 wt.% to demonstrate the effect of polymer orientation as seen from the bottom spectra of Figure 4.11. The predicted direction of alignment was parallel to the radial direction, which is clearly matching with the significantly increased intensity of PMMA peaks of that spectrum. Clearly, all peaks are canceled out in the spectrum perpendicular to the radial direction, indicating a high amount of aligned polymers. For both orientations, switching to non-polarized light would result in the appearance of all expected peaks. PMMA chains aligned perpendicular to the direction of heat conduction would lower thermal conductivity, thus it is important to ensure that all samples have the desired degree of alignment. Spectra for annealed polymer films from 750k PMMA - 5 wt.% reveal no alignment for neither high nor low spin speeds, indicating that isotropic PMMA can be expected for the 3ω models fabricated herein. Indeed, none of the >10 investigated samples showed signs of polymer alignment. Similarly non-polarized spectra revealed no differences in polymer structure, indicating that 750k PMMA - 5 wt.% films are indeed suitable for finding TBC from the 3ω method. The added relative intensity of the 810 cm^{-1} peak observed for all dissolved samples has yet to be explained, but indicates some difference in polymer structure after processing.

For forthcoming thermal measurements it can be of interest to compare the properties of aligned and unaligned polymer films. The presented results indicate that solutions of low concentration do not present sufficient viscosity for chain alignment to occur during spin coating. However, the orientation of unannealed, dilute films spun at speeds >2000 rpm was not investigated, thus there may still be a possibility for fabrication of anisotropic PMMA thin films. Extending exposure times allows for good signal-to-noise ratio of films down to nm thickness, allowing all polymer films

to be checked for both chemical and orientational changes. As intensity is linearly correlated to the amount of probed material, an appropriate calibration standard should also allow the non-destructive measurement of film thickness with µm lateral resolution [72].

5.6 Metal structure

Spherical cap shaped surface features presented in Figures 3.3, 4.12 and 4.14 are indicative of columnar growth modes as presented in Chapter 2.4 and more directly observed for 360 nm thick Au films [41]. As cross-section imaging was not pursued, defects in these columnar grain structures can only be assumed to be similar to what was imaged by Zhou et al. [41]. Grains may have less defects due to the added energy of the sputtering process. The effect of sputtering is also seen by comparing surface features, where the surprisingly compact structure of the mapped metal films with low roughness is indicative of zone T growth where grain columns are embedded in an amorphous matrix as opposed to voids.

The lack of change when moving from PMMA to Si/Ti substrates indicates that the surface structure of thicker Au films are independent of the substrate for DC magnetron sputtering at ambient temperature. Similarly, a comparison of height maps, yields R_a for all films in the 1 to 1.5 nm range with no particular relation to film thickness. Such smooth films are clearly below the 15 nm limit for sufficient specular reflection in thermoreflectance measurements [2]. For 3ω samples, where the interesting interface is that between spuncast PMMA and Au, the polymer is expected to conform to the smooth surface [48].

Similarities in film morphology on the substrate side is also expected on the interface side due to similar nucleation and growth models for both Si and PS substrates [38, 40]. Indeed, adhesion tests presented herein have revealed Au on both Si, SiO_2 and PMMA to have similar low substrate adhesion in line with results reported by Min et al. [50]. Investigations of how the polymer-metal interface evolves with film thickness above 20 nm have not been conducted as this interface is generally unavailable. Here is seen a discrepancy between observed adhesion and literature models for the metal-polymer interface. According to Schwartzkopf et al. metal nuclei grow laterally to fill the entire surface, implicating the absence of interface voids, identical to what is expected for spuncast polymer films. However, spuncast polymer films exhibit much stronger adhesion to Au films compared to the case of Au sputter coated on PMMA.

To investigate this discrepancy, AFM height maps were captured of the interface side of a sputter deposited Au film peeled from a PMMA sheet. The comparison of both sides of a Au film seen in Figure 4.13 is, to the author's knowledge, the first time investigation of the underside of a peeled metal thin film have been used to investigate ambient temperature metal nucleation. Figure 4.13a and Figure 4.12e which are maps of the same metal film separated in time by three months and in method by the use of a 100 times stiffer cantilever in the second case. Comparing the two, it is clear that the feature sizes are similar, indicating little morphology change with time, an effect that is validated by comparing height maps of different resolutions. By calculating roughness for two height maps of identical size and sample it is clear that the two different cantilevers yields the same roughness for these samples. Thus, the morphology measurements by AFM of metal films on soft substrates is not adversely affected by the use of a stiff cantilever.

The two images of Figure 4.12 seem to correlate with the general SZM, where the film grows from nucleation sites on the substrate that evolves in size to form columnar grains. However, the complete filling of the substrate with intimate contact as expected from the growth model by Kaune et al. is not observed. The present results lean towards a model of less metal-polymer interaction, where initial nuclei grow little before acting as nucleation sites for new grains that grow vertically and laterally, filling the area above the substrate without necessarily touching it. Vertical growth is subsequently initiated with accompanying grain growth as the film thickness increases, forming columnar structures with spherical caps observed on the surface. Thus, the observed voids are left behind in the interface, with only the initial nuclei touching the polymer, reducing the actual interface area. A reduction in actual interface area will cause lower TBC as there are fewer physical and chemical bonds to transport vibrational energy. The apparent tilt in the direction of the features may be explained by the rough peeling by hand that likely imparted some lateral force on the interface. Discrepancy between these observations and those of Schwartzkopf et al. may be due to the PS-Au interaction energy being stronger than that of PMMA-Au. This assumption is supported by higher adhesion between Cu and plasma exposed PS compared to Cu and plasma exposed PMMA [47]. Ruffino et al., however, calculated work of adhesion and found PMMA to interact more strongly than PS to Au [35].

The observed rough interface structure explains the observed adhesion difference between the two interface fabrication routes. It is also clear that steps should be taken to improve interface coverage to ensure that the measured TBC is a material property and not an effect of a rough interface.

5.7 Carbon coating

Successful carbon coating by evaporation is verified by the µ-Raman spectrum shown in Figure 4.9g, but the coating is not homogeneous in thickness, likely due to the observed crudeness of the deposition method. The allotrope of deposited carbon is non-hydrogenated and graphite-like as seen by comparing to Figure 1 and 6 of [73], keeping in mind the D and G peak positions of resepctively, 1340 and 1575 cm^{-1}. µ-Raman microscopy is thus proven to be a useful tool in evaluating the distribution and allotrope of deposited carbon thin films. It can also be used for carbon deposited on PMMA films as they do not have overlapping peaks. Adhesion was not observed to lessen with the application of carbon, thus it is still a promising candidate as a TBC enhancing layer. However, the crude method, the uneven coverage and the amorphous nature of the deposited carbon all demonstrate the need for testing other methods of carbon deposition. If carbon is to be deposited onto PMMA, structural and chemical effects of the deposition method on the polymer should also be monitored.

5.8 PVA release layer and QSTF model systems

Initial trials with PVA have proven the water release method to be a promising route for ultra-gentle peeling. Next, it should be verified that all PVA is indeed removed during water immersion, possibly by Raman spectroscopy or AFM given that remaining structures are larger than single macromolecules. Immersion in water at 25 °C affects PMMA thin films by creating a hydrated substrate interface layer as well as increasing the bulk water content to about 5 % [74]. Efforts to avoid delamination of PMMA-Cu films in step 4 of Figure 2.6e and drying of PMMA should therefore be made. If successful, this water release method may prove to be useful in a range of novel fabrication strategies and could potentially facilitate AFM characterization of metal-polymer interfaces for even well-adhering metal layers. If the above-mentioned difficulties are not overcome, strategies similar to the ones utilized by Jiao et al. may prove useful both to release PMMA from Si substrates and to gently remove PMMA for the study of as-deposited metal interface structures [53].

5.9 Metal-polymer interface properties

So far, acceptable control over polymer and metal structure has been demonstrated, as well as the interface between metal and spuncast polymer films. This interface is special as the metal surface can be easily characterized before spincoating and the polymer is expected to cover the surface completely and with sufficient drying, no solvent or water contamination should be present.

Four interface characteristics were mentioned in Figure 2.5:

- Morphology
- Presence of voids
- Contamination or deliberate addition of interface layers
- Chemical or physical bonds in the interface or in the dual interface created by contamination or interface layers

Morphology and presence of voids are apparently intimately linked, as some fabrication routes may fill out voids in rough surfaces, whereas others will not. Interface morphology beneath transparent layers are clearly accessible by VSI or VXI. For other systems, gentle removal of one layer should permit characterization of the interface and comparison to preferably quantitative adhesion tests could reveal whether the two materials are in intimate contact.

Presence of deliberately added non-metallic materials in the interface can likely be quantified and mapped by Raman spectroscopy as already demonstrated for the carbon coating. Metal adhesion layers or minute chemical changes would however require other techniques, possibly X-ray reflectometry for density and thickness of metal layers and X-ray photoelectron spectroscopy (XPS) for chemical changes. XPS is common in TBC studies as it allows surface sensitive detection and quantification of interface bonds, being potentially the only method for accurately probing this feature [8, 13].

The most direct method for probing all mentioned interface features simultaneously is adhesion testing. For cases where single parameters are varied systematically, quantitative adhesion testing could be equally important to more complex spectroscopic characterizations. Jin et al. utilized a simple setup where shadow-mask deposited test patterns were peeled and the type of adhesion failure and any remaining material was analyzed [8]. 90° pull testing using force transducers glued to metal thin films have also been demonstrated to be effective [47]. Scratch testing could also be utilized, but analysis have proven difficult, at least for the case of ductile metal films well adherent to soft substrates [1]. It is also important that the glue is

not the point of failure as often observed herein, as the mode of failure can not be determined in such cases.

6 Conclusion

The focus of this thesis work has been to develop laminar model systems for forthcoming characterization of TBC by three different methods, namely frequency domain thermoreflectance, 3-omega and quasi-static thermal flow. Two different models for FDTR characterization were demonstrated, one 100 nm Au thin film on PMMA bulk and one Si-PMMA(23 nm)-Au (50 nm) stack. A proof of concept was developed for a third model system, where PMMA was melted onto a 100 nm Au film followed by peeling of the same film. Rapid fabrication and characterization of a Si(dry etched)-Ti(20 nm)-Au(500 nm)-PMMA(400-800 nm) 3ω model system comprising five different film thicknesses was demonstrated. Vertical scanning interferometry proved to be a rapid and accurate method for finding polymer thickness from films with smooth step edges. These step edges were created by a specially developed batch fabrication technique of selective film removal by immersing in acetone. For films thinner than 130 nm, AFM was used to accurately measure thickness down to at least 20 nm. QSTF models were not completed, but vital steps such as transfer printing of metal-polymer laminates and release of spincoated PMMA films were demonstrated with the available tools.

In addition to sample fabrication, efforts were made to understand metal and polymer internal structure based on both literature and original experiments. Reverse side AFM mapping of a sputtered Au film was, to the authors knowledge, used to characterize ambient temperature metal growth for the first time. Contrary to expectations, nanoscale interface voids were observed in the obtained maps, explaining poor adhesion between polymer substrates and sputtered metal films. Interface side

topography maps, together with quantitative nanomechanical mapping and SEM imaging of metal surfaces were employed to elucidate a metal structure comprising columnar grains with few voids and a rough interface side. Lateral size of surface features were observed to evolve with thickness, seemingly independent of substrate, metal and deposition speed, although a more detailed study is warranted. Metal roughness was seen to be largely independent of thickness and substrate, and was deemed sufficiently low for all thermal characterization methods, however, e-beam evaporation was found to yield too rough films. μ-Raman spectroscopy was shown to be an invaluable tool capable of observing changes in polymer structure and molecular chain alignment and used to prove that spincoated 300 to 800 nm PMMA films had identical internal structure. μ-Raman spectroscopy was also used to characterize a nm thick evaporated carbon layer, indicating its usefulness for carbon-based surface modifications.

The methods and model systems developed herein will be of importance for future work in this exciting field.

Further work

Some model systems have yet to be completed and no systems have yet been used in thermal characterization, thus new problems may yet arise. This work have also touched upon other very interesting directions of study, although not directly useful to the HEFACE project.

3-omega

A rigorous method for detecting and avoiding pinholes during 3ω sample fabrication is needed as metal embedded on the large surface area of the breakout pads may cause a short circuit in case of any pinholes. Suggested improvements to roughness and defect measuring protocol of using the VXI mode and simultaneously capturing high resolution images of the whole sample surface should improve the situation.

Film thickness

The current solvent immersion method for fabricating step edges for thicker films should be upgraded by the use of a computer controlled arm for dipping. Ideally, other methods of accurate thickness measurements, preferably non-invasive and with good lateral resolution should be investigated. Ellipsometry and µ-Raman spectroscopy have been mentioned as promising instruments, the latter being more demanding to realize. Verification of metal film thickness is also lacking. In this case, X-ray reflectometry is regarded as the optimal choice to non-destructively characterize both thickness and density.

Thin polymer films

Controlled fabrication of uniform, defect-free films <100 nm have yet to be realized. Such films will be necessary for QSTF characterization and may also prove useful for the FDTR and 3ω methods, if the current TBC sensitivity is found to be too low and very thin films [18] or multilayer stacks [8] are required. Thickness, uniformity,

defect concentration and changes in mechanical properties can be measured by AFM in the PF-QNM mode. However, once a protocol has been made and all properties of produced polymer films are known, ellipsometry would prove a faster method for determining film thickness.

Completing QSTF samples

Fabricating a complete set of QSTF samples is dependent upon defect-free sub 100 nm thin films. The PVA release method needs further investigations, such as remaining PVA after release, minimum PMMA thickness, and effect of water on spuncast PMMA. An alternative release method is that of Jiao et al., where spuncast PMMA is immersed in 1 mol dm^{-3} potassium hydroxide at 80 °C to slightly hydrolyze the PMMA [53]. If double-sided metal coating of such films are found hard to realize, the more facile route of having one interface from spincoating and one from sputter coating should be pursued. Modeling the interfaces as having separate TBC, multilayer stacks could be batch fabricated to improve sensitivity.

Improving adhesion of sputtered metal

Adhesion and uniformity of metal coatings should be pursued in the interest of studying TBC of interfaces free of voids. By pursuing the double-sided AFM inquiry, new knowledge of metal growth on polymer interfaces could be obtained. This path may require dissolving PMMA as opposed to peeling in order to also access well adherent metal films. Metal adhesion layers, carbon or silk protein are facile routes of interface improvement, but also add complexity to the system in terms of fabrication, measurement modeling and simulation. Ideally, metal deposition onto polymers or interface layers could be avoided altogether for most model systems by spincoating onto metal layers followed by peeling, a technique which has already proven to yield good adhesion. Metal sputtering could then be performed at higher temperatures and without fear of damaging the PMMA surface.

Other sample characterization tools

X-ray photoelectron spectroscopy should prove a good method for measuring chemical bonds at surfaces and interfaces due to high surface sensitivity. Development of quantitative adhesion testing is also absolutely necessary as a rapid method for testing all the interesting properties of the interface simultaneously. Based on adhesion

data, further characterization could be done to determine the relative effects of each interface property.

Bibliography

[1] Birger Langebro and Jianying He. Synthesis and multiphysical characterization of metal-polymer thin films. Report, Norwegian University of Science and Technology, Trondheim, 2017.

[2] David G Cahill, Paul V Braun, Gang Chen, David R Clarke, Shanhui Fan, Kenneth E Goodson, William P King, Gerald D Mahan, Arun Majumdar, Humphrey J Maris, Simon R Phillpot, Eric Pop, David G Cahill, Paul V Braun, Gang Chen, David R Clarke, Shanhui Fan, Kenneth E Goodson, Pawel Keblinski, William P King, Gerald D Mahan, Arun Majumdar, Humphrey J Maris, Simon R Phillpot, Eric Pop, and Li Shi. Nanoscale thermal transport . II . 2003 – 2012. *Applied Physics Reviews 1*, 011305(2014), 2014.

[3] Arden L. Moore and Li Shi. Emerging challenges and materials for thermal management of electronics. *Materials Today*, 17(4):163–174, 2014.

[4] Christian Monachon, Ludger Weber, and Chris Dames. Thermal Boundary Conductance: A Materials Science Perspective. *Annual Review of Materials Research*, 46(1):433–463, 2016.

[5] Wee-Liat Ong, Sara M. Rupich, Dmitri V. Talapin, Alan J. H. McGaughey, and Jonathan A. Malen. Surface chemistry mediates thermal transport in three-dimensional nanocrystal arrays. *Nature Materials*, 12(5):410–415, 5 2013.

[6] Firman Bagja Juangsa, Yoshiki Muroya, Meguya Ryu, Junko Morikawa, and Tomohiro Nozaki. Comparative study of thermal conductivity in crystalline and amorphous nanocomposite. *Applied Physics Letters*, 110:253105, 6 2017.

[7] Elbara Ziade, Miguel Goni, Toshiyuki Sato, Pawel Czubarow, and Aaron J. Schmidt. Thermal conductance of nanoscale Langmuir-Blodgett films. *Applied Physics Letters*, 107(22), 2015.

[8] Yansha Jin, Chen Shao, John Kieffer, Kevin P. Pipe, and Max Shtein. Origins of thermal boundary conductance of interfaces involving organic semiconductors. *Journal of Applied Physics*, 112(9):093503, 11 2012.

[9] Jeffrey L. Braun, Sean W. King, Ashutosh Giri, John T. Gaskins, Masanori Sato, Takemasa Fujiseki, Hiroyuki Fujiwara, and Patrick E. Hopkins. Breaking network connectivity leads to ultralow thermal conductivities in fully dense amorphous solids. *Applied Physics Letters*, 109:191905, 2016.

[10] Mark D. Losego and David G. Cahill. Thermal transport: Breaking through barriers. *Nature Materials*, 12(5):382–384, 2013.

[11] Hamid Reza Seyf, Luke Yates, Thomas L Bougher, Samuel Graham, Baratunde A Cola, Theeradetch Detchprohm, Mi-Hee Ji, Jeomoh Kim, Russell Dupuis, Wei Lv, and Asegun Henry. Rethinking phonons: The issue of disorder. *npj Computational Materials*, 3:49, 2017.

[12] Xu Xie, Dongyao Li, Tsung-Han Tsai, Jun Liu, Paul V. Braun, and David G. Cahill. Thermal Conductivity, Heat Capacity, and Elastic Constants of Water-Soluble Polymers and Polymer Blends. *Macromolecules*, 49(3):972–978, 2016.

[13] Mark D. Losego, Martha E. Grady, Nancy R. Sottos, David G. Cahill, and Paul V. Braun. Effects of chemical bonding on heat transport across interfaces. *Nature Materials*, 11(6):502–506, 2012.

[14] Minyoung Jeong, Justin P. Freedman, Hongliang Joe Liang, Cheng Ming Chow, Vincent M. Sokalski, James A. Bain, and Jonathan A. Malen. Enhancement of Thermal Conductance at Metal-Dielectric Interfaces Using Subnanometer Metal Adhesion Layers. *Physical Review Applied*, 5(1):1–7, 2016.

[15] Woosung Park, Aditya Sood, Joonsuk Park, Mehdi Asheghi, Robert Sinclair, and Kenneth E. Goodson. Enhanced Thermal Conduction Through Nanostructured Interfaces. *Nanoscale and Microscale Thermophysical Engineering*, 21 (3):134–144, 2017.

[16] Yanguang Zhou, Xiaoliang Zhang, and Ming Hu. An excellent candidate for largely reducing interfacial thermal resistance: a nano-confined mass graded interface. *Nanoscale*, 8(4):1994–2002, 1 2016.

[17] Sigurd R. Pettersen, Shijo Nagao, Helge Kristiansen, Susanne Helland, John Njagi, Katsuaki Suganuma, Zhiliang Zhang, and Jianying He. Investigation of

thermal transport in polymer composites with percolating networks of silver thin films by the flash diffusivity method. *Journal of Applied Physics*, 121(2): 025101, 2017.

[18] Mark D. Losego, Lionel Moh, Kevin A. Arpin, David G. Cahill, and Paul V. Braun. Interfacial thermal conductance in spun-cast polymer films and polymer brushes. *Applied Physics Letters*, 97(1):011908, 2010.

[19] Bryan C. Gundrum, David G. Cahill, and Robert S. Averback. Thermal conductance of metal-metal interfaces. *Physical Review B*, 72(24):245426, 12 2005.

[20] Wei Wang and David G. Cahill. Limits to Thermal Transport in Nanoscale Metal Bilayers due to Weak Electron-Phonon Coupling in Au and Cu. *Physical Review Letters*, 109(17):175503, 10 2012.

[21] David G Cahill and R O Pohl. Thermal conductivity of amorphous solids above the plateau. *Physical Review B*, 35(8):4067–4073, 1987.

[22] Juliana Jaramillo Fernandez. *Tuning the thermal conductivity of polycrystalline films via multiscale structural defects and strain*. PhD thesis, Ecole Centrale Paris, 2015.

[23] Aaron J. Schmidt, Ramez Cheaito, and Matteo Chiesa. A frequency-domain thermoreflectance method for the characterization of thermal properties. *Review of Scientific Instruments*, 80(9):094901, 2009.

[24] David G. Cahill. Analysis of heat flow in layered structures for time-domain thermoreflectance. *Review of Scientific Instruments*, 75(12):5119–5122, 12 2004.

[25] Dietrich Meyerhofer. Characteristics of resist films produced by spinning. *Journal of Applied Physics*, 49(7):3993–3997, 1978.

[26] Christopher B. Walsh and Elias I. Franses. Ultrathin PMMA films spin-coated from toluene solutions. *Thin Solid Films*, 429(1-2):71–76, 2003.

[27] T. Tippo, C. Thanachayanont, P. Muthitamongkol, C. Junin, M. Hietschold, and A. Thanachayanont. The effects of solvents on the properties of ultra-thin poly (methyl methacrylate) films prepared by spin coating. *Thin Solid Films*, 546: 180–184, 2013.

[28] Christoph O. Blattmann and Sotiris E. Pratsinis. In situ measurement of conductivity during nanocomposite film deposition. *Applied Surface Science*, 371: 329–336, 2016.

[29] N. G. Semaltianos. Spin-coated PMMA films. *Microelectronics Journal*, 38 (6-7):754–761, 2007.

[30] Niranjan Patra, Alberto C. Barone, and Marco Salerno. Solvent effects on the thermal and mechanical properties of poly(methyl methacrylate) casted from concentrated solutions. *Advances in Polymer Technology*, 30(1):12–20, 3 2011.

[31] Nanshu Lu, Xi Wang, Zhigang Suo, and Joost Vlassak. Metal films on polymer substrates stretched beyond 50%. *Applied Physics Letters*, 91(22):221909, 2007.

[32] J. Musil. Flexible hard nanocomposite coatings. *RSC Advances*, 5(74):60482–60495, 2015.

[33] Julian Quirk and Michael Serda. *Semiconductor Manufacturing Technology*. Prentice Hall, 2001. ISBN 0-13-081520-9.

[34] Louis Hornyak, H F Tibbals, Joydeep Dutta, and J J. Moore. *Introduction to Nanoscience and Nanotechnology*. Taylor & Francis Group, Boca Raton, 2 edition, 2008. ISBN 978-1-4200-4779-0.

[35] F. Ruffino, V. Torrisi, G. Marletta, and M. G. Grimaldi. Growth morphology of nanoscale sputter-deposited Au films on amorphous soft polymeric substrates. *Applied Physics A: Materials Science and Processing*, 103(4):939–949, 2011.

[36] F. Ruffino, V. Torrisi, G. Marletta, and M. G. Grimaldi. Effects of the embedding kinetics on the surface nano-morphology of nano-grained Au and Ag films on PS and PMMA layers annealed above the glass transition temperature. *Applied Physics A: Materials Science and Processing*, 107(3):669–683, 2012.

[37] Gunar Kaune, Matthias A Ruderer, Ezzeldin Metwalli, Weinan Wang, Sebastien Couet, Kai Schlage, Ralf Rohlsberger, Stephan V Roth, and Peter Muller-Buschbaum. In Situ GISAXS Study of Gold Film Growth on Conducting Polymer Films. *ACS Applied Materials & Interfaces*, 1(2):353–360, 2009.

[38] Matthias Schwartzkopf, Adeline Buffet, Volker Korstgens, Ezzeldin Metwalli, Kai Schlage, Gunthard Benecke, Jan Perlich, Monika Rawolle, André Rothkirch, Berit Heidmann, Gerd Herzog, Peter Muller-Buschbaum, Ralf

Rohlsberger, Rainer Gehrke, Norbert Stribeck, and Stephan V. Roth. From atoms to layers: in situ gold cluster growth kinetics during sputter deposition. *Nanoscale*, 5(11):5053–5062, 2013.

[39] Matthias Schwartzkopf, Gonzalo Santoro, Calvin J. Brett, André Rothkirch, Oleksandr Polonskyi, Alexander Hinz, Ezzeldin Metwalli, Yuan Yao, Thomas Strunskus, Franz Faupel, Peter Müller-Buschbaum, and Stephan V. Roth. Real-Time Monitoring of Morphology and Optical Properties during Sputter Deposition for Tailoring Metal-Polymer Interfaces. *ACS Applied Materials and Interfaces*, 7(24):13547–13556, 2015.

[40] Matthias Schwartzkopf, Alexander Hinz, Oleksandr Polonskyi, Thomas Strunskus, Franziska C. Löhrer, Volker Körstgens, Peter Müller-Buschbaum, Franz Faupel, and Stephan V. Roth. Role of Sputter Deposition Rate in Tailoring Nanogranular Gold Structures on Polymer Surfaces. *ACS Applied Materials and Interfaces*, 9(6):5629–5637, 2017.

[41] Shujun Zhou, Wei Wu, and Tianmin Shao. Effect of post deposition annealing on residual stress stability of gold films. *Surface and Coatings Technology*, 304: 222–227, 2016.

[42] John A Thornton. High rate thick film growth. *Annual Review of Materials Science*, 7:239–260, 1977.

[43] Rongying Huang, Yang Cao, and Hong Qiu. Structural and electrical properties of Au films sputter-deposited on HCl-doped polyaniline substrates. *Thin Solid Films*, 583:158–162, 5 2015.

[44] Nanshu Lu, Xi Wang, Zhigang Suo, and Joost Vlassak. Failure by simultaneous grain growth, strain localization, and interface debonding in metal films on polymer substrates. *Journal of Materials Research*, 24(02):379–385, 2009.

[45] Nanshu Lu, Zhigang Suo, and Joost J. Vlassak. The effect of film thickness on the failure strain of polymer-supported metal films. *Acta Materialia*, 58(5): 1679–1687, 2010.

[46] Jerry L. Atwood and Jonathan W. Steed. *Supramolecular chemistry*. Wiley, 2013. ISBN 9781118681503.

[47] V. Zaporojtchenko, J. Zekonyte, and F. Faupel. Effects of ion beam treatment on atomic and macroscopic adhesion of copper to different polymer materials. *Nuclear Instruments and Methods in Physics Research, Section B: Beam Interactions with Materials and Atoms*, 265(1):139–145, 2007.

[48] Carol Ochoa-Putman and Uday K. Vaidya. Mechanisms of interfacial adhesion in metal–polymer composites – Effect of chemical treatment. *Composites Part A: Applied Science and Manufacturing*, 42(8):906–915, 8 2011.

[49] V. Zaporojtchenko, J. Zekonyte, S. Wille, U. Schuermann, and F. Faupel. Tailoring of the PS surface with low energy ions: Relevance to growth and adhesion of noble metals. *Nuclear Instruments and Methods in Physics Research, Section B: Beam Interactions with Materials and Atoms*, 236(1-4):95–102, 2005.

[50] Kyungtaek Min, Muhammad Umar, Shinyoung Ryu, Soonil Lee, and Sunghwan Kim. Silk protein as a new optically transparent adhesion layer for an ultra-smooth sub- 10nm gold layer. *Nanotechonolgy*, 28:115201, 2017.

[51] Matthew A. Meitl, Zheng Tao Zhu, Vipan Kumar, Keon Jae Lee, Xue Feng, Yonggang Y. Huang, Ilesanmi Adesida, Ralph G. Nuzzo, and John A. Rogers. Transfer printing by kinetic control of adhesion to an elastomeric stamp. *Nature Materials*, 5(1):33–38, 2006.

[52] Filippo Pizzocchero, Lene Gammelgaard, Bjarke S. Jessen, José M. Caridad, Lei Wang, James Hone, Peter Bøggild, and Timothy J. Booth. The hot pick-up technique for batch assembly of van der Waals heterostructures. *Nature Communications*, 7(11894), 2016.

[53] Liying Jiao, Ben Fan, Xiaojun Xian, Zhongyun Wu, Jin Zhang, and Zhongfan Liu. Creation of Nanostructures with Poly (methyl methacrylate) -Mediated Nanotransfer Printing. *Journal of American Chemical Society Communications*, 130(38):1–8, 2008.

[54] Peter de Groot. Principles of interference microscopy for the measurement of surface topography. *Advances in Optics and Photonics*, 7(1):1–65, 3 2015.

[55] Yiping Zhao, Gwo-Ching Wang, and Toh-Ming Lu. *Characterization of Amorphous and Crystalline Rough Surface–Principles and Applications*. Academic press, 2000. ISBN 9780124759848.

[56] G. Binnig and C. F. Quate. Atomic Force Microscope. *Physical Review Letters*, 56(9):930–933, 1986.

[57] Franz J. Giessibl. Advances in atomic force microscopy. *Reviews of Modern Physics*, 75(3):949–983, 2003.

[58] Farid F. Abraham, Inder P. Batra, and S. Ciraci. Effect of tip profile on atomic-force microscope images: A model study. *Physical Review Letters*, 60(13): 1314–1317, 1988.

[59] Pavel Trtik, Josef Kaufmann, and Udo Volz. On the use of peak-force tapping atomic force microscopy for quantification of the local elastic modulus in hardened cement paste. *Cement and Concrete Research*, 42(1):215–221, 2012.

[60] Bede Pittenger, Natalia Erina, and Chanmin Su. Quantitative Mechanical Property Mapping at the Nanoscale with PeakForce QNM. *Burker Application Note*, 128:1–12, 2009.

[61] Matt Novak. VXI Universal Surface Measurements for 3D Optical Microscopes. Report, Bruker Nano Surfaces Divison, Tucson, Arizona, 2013. URL `https://mbns.bruker.com/acton/attachment/9063/f-09b6/0/-/-/-/-/AN554-VXI.pdf_blank`.

[62] Fotis Kossivas, Charalabos Doumanidis, and Andreas Kyprianou. Thickness Measurement of Photoresist Thin Films Using Interferometry. In Dr. Ivan Padron, editor, *Interferometry - Research and Applications in Science and Technology*, pages 361–376. InTech, 3 2012.

[63] Chin Y. Poon and Bharat Bhushan. Comparison of surface roughness measurements by stylus profiler, AFM and non-contact optical profiler. *Wear*, 190(1): 76–88, 1995.

[64] Chandrasekhara Venkata Raman and Kariamanikkam Srinivasa Krishnan. A new type of secondary radiation. *Nature*, 121(3048):501–502, 1928.

[65] A. H. Kuptsov and G. N. Zhizhin. *Handbook of fourier transform Raman and infrared spectra of polymers*. Elsevier, 1998. ISBN 0080531946.

[66] M. Tanaka and R. J. Young. Review Polarised Raman spectroscopy for the study of molecular orientation distributions in polymers. *Journal of Materials Science*, 41(3):963–991, 2 2006.

[67] Jamie J Gengler, Sukesh Roy, John G Jones, and James R Gord. Two-color time-domain thermoreflectance of various metal transducers with an optical parametric oscillator. *Measurement Science and Technology*, 23(5):055205, 5 2012.

[68] S. U. Campisano, G. Foti, F. Grasso, and E. Rimini. Ion Backscattering Analysis of Mixing in Au–Cu and Au–Al Thin Films. *Japanese Journal of Applied Physics*, 13(S1):637, 1 1974.

[69] J. Bavier, J. Cumings, and D. R. Hines. Transfer printing of patterned metal films using parylene C coated surfaces. *Microelectronic Engineering*, 104: 18–21, 2013.

[70] Paul H C Eilers and Hans F M Boelens. Baseline Correction with Asymmetric Least Squares Smoothing. Report, Leiden University Medical Centre, Leiden, 2005. URL `https://zanran_storage.s3.amazonaws.com/www.science.uva.nl/ContentPages/443199618.pdf`.

[71] Youngjun Yun, Christopher Pearson, and Michael C. Petty. Pentacene thin film transistors with a poly(methyl methacrylate) gate dielectric: Optimization of device performance. *Journal of Applied Physics*, 105(3):034508, 2009.

[72] Barbara M. Liszka, Aufried T. M. Lenferink, Geert-Jan Witkamp, and Cees Otto. Raman micro-spectroscopy for quantitative thickness measurement of nanometer thin polymer films. *Journal of Raman Spectroscopy*, 46(12):1230–1234, 12 2015.

[73] M. A. Tamor and W. C. Vassell. Raman “fingerprinting” of amorphous carbon films. *Journal of Applied Physics*, 76(6):3823–3830, 9 1994.

[74] Peter W. Akers, Andrew R.J. Nelson, David E. Williams, and Duncan J. McGillivray. Formation of hydrated layers in PMMA thin films in aqueous solution. *Applied Surface Science*, 353:829–834, 10 2015.

Postscript

After the thesis was nearly completed, samples prepared for the 3-omega method proved to have defects that caused a short-circuit to the metal coated substrate. As there were some extra time before the thesis deadline, it was decided that new samples should be fabricated. A new model for 3ω data interpretation, taking into account the boundary conductance of the interface between 3ω metal wire and polymer film was also discovered, eliminating the need for a metal coated substrate. New samples could therefore be produced very simply as a Si/SiO_x/PMMA laminate to be coated with the 3ω structure after shipping to Spain. Evidently, defect characterizing methods were not sensitive to these pin-holes, or pin-holes may have been formed during packing and shipping before final metal deposition. The new sample fabrication route should therefore also take care to develop the characterization tools to amply detect defects. In the following, methods are detailed thoroughly so as to function as a protocol for future sample fabrication.

Materials & methods

Cell-cast PMMA sheets of nominal thickness 1.1 mm and estimated mass average molecular weigh ($\overline{M}_w$) 500 000-1 000 000 were acquired from Goodfellow Cambridge Ltd. Anisole (A-thinner) was acquired from MicroChem Corp and freshly opened. 4 in Si wafers were acquired from UniversityWafer Inc. All work was performed in a clean-room facility under ISO 7 conditions.

Flasks were prepared by washing thrice in IPA, drying in a stream of nitrogen and washing thrice in small amounts of anisole, noting the final weight of anisole wetting the bottle and lid. PMMA sheets diced to 1 cm $\times$ 1 cm pieces were washed in ethanol and dried on a hot-plate at 90 °C before adding to a washed bottle. Anisole was added to fill the bottle and concentration in wt.% was noted. Dissolving PMMA proceeded by repeating a process of manual shaking, ultrasonication at 45 °C for a total of 2 hours and stirring vigorously overnight for a total of 2 days. Diluting

solutions was performed by filtering the original solution through a 0.2 μm syringe filter into a new thrice washed bottle and adding anisole to desired concentration.

A Bruker Contour GT-K optical profiler was to capture grayscale images of entire sample surfaces, using the automated stitching function of the accompanying Vision64™ software. Images were captured with 20 % image-to-image overlap using a 2.5x objective, with the surface slightly out of focus to avoid image saturation of the interference fringes. Grayscale values were automatically normalized and mapped to a blue-red color spectrum by the software, before saving in the lossless *portable network graphics* format, which was the only provided option.

Si wafers with native SiO_x oxide were rinsed in isopropyl alcohol (IPA) and dried in a stream of nitrogen. Dicing to 1 cm $\times$ 1 cm chips was done using a scriber to apply a single scratch on the wafer back-side, guided by a ruler and a wafer breaking tool to create the momentum needed to break the wafer. Scratches were applied to not intersect with wafer edges to avoid edge fracturing. Initially, the breaking tool was pressed directly onto the wafer, later a tissue and eventually scotch tape was applied to protect the wafer surface.

Si chip washing steps investigated in various combinations were:

1. Rinsing in IPA and drying in a stream of nitrogen.
2. Ultrasonicating in acetone followed by IPA for 10 min each and drying in a stream of nitrogen.
3. Ultrasonicating in water for 10 min before rinsing in IPA and drying in a stream of nitrogen.
4. O_2 plasma clean for 3 min.
5. Baking on a hot-plate at 180 °C for 10 min.

Conveniently, a chip carrier in which 11 chips of this minute size could be mounted vertically, was available for liquid immersion steps.

Prior to spincoating, Si chips where baked on a hotplate at 180 °C for at least 5 min before cooling rapidly and attaching to a larger chip using double sided thermal release tape and removing dust in a stream of nitrogen. The larger carrier chip was needed as chucks for chips smaller than 1.5 cm were not available for the SÜSS LabSpin spincoater used herein. 2-3 drops PMMA solution from a plastic pipette was dispensed to cover the chip surface before accelerating at 2000 rpm/s to 2000 rpm and holding for 45 s. Carrier chips were subsequently placed on a hotplate at 180 °C for some seconds to activate the thermal release tape before rapidly cooling the PMMA-coated chips to minimize heating. Softbaking at 180 °C was performed for some chips.

As Si dust was later deemed the most prevalent source of contamination, extreme care was taken to avoid additional contamination after dicing, replacing metal tweezers for plastic tweezers where possible. 4×4 chip trays used for convenient batch handling were lined with pieces of tape to avoid vacuum formation between flat tray bottom and flat chip backside.

After completion of the thesis work, the stylus profilometer received substantial maintenance allowing it to repeatably and rapidly measure step heights of all produced films. Steps were produced by scraping with a sharp plastic cocktail stick in a straight line from the center of each chip to be investigated. Successful step fabrication could be verified from reflectivity contrast by eye for all produced films (i.e. down to 10 nm thickness). The 6.5 µm radius stylus of the Veeko Dektak150 profilometer was scanned 200 to 400 µm of the surface, moving at $25\,\mu m\,s^{-1}$ with a contact force of 10 mg. Step height was manually measured from the region immediately adjacent to the step edge for 3 to 11 different individual scans along the scratch.

After completed fabrication, chips were packed in 4×4 plastic chip trays by attaching to double sided tape on the tray bottom. After a short investigation, pressing on chip corners with glove-covered nails was found to be the best method for securing chips to the tape with minimal film damage. Chip trays were subsequently placed in zip-lock bags in the hope of avoiding as much contamination as possible, before shipping to Spain.

Results & discussion

Both software enhanced vertical scanning interferometry and phase scanning interferometry were found not to be very sensitive to surface contamination and defects. These defects were very clear in the grayscale intensity images captured by the optical profiler, therefore it was decided that such images were preferred. The defocus needed to avoid interference fringes did not significantly blur features as the 2.5x objective had a large depth of focus. In this fashion, stitched high resolution images of an entire $1\,cm \times 1\,cm$ sample surface as seen in Figure P.1a could be captured in $\sim$2 min. Additionally, images of several chips could be captured without operator supervision utilizing the advanced batch automation tools of the software. This method of chip imaging is a great improvement over manual inspection in an optical microscope, improving speed and reportability significantly.

From comparing a wafer before and after dicing, it was clear that dicing produced

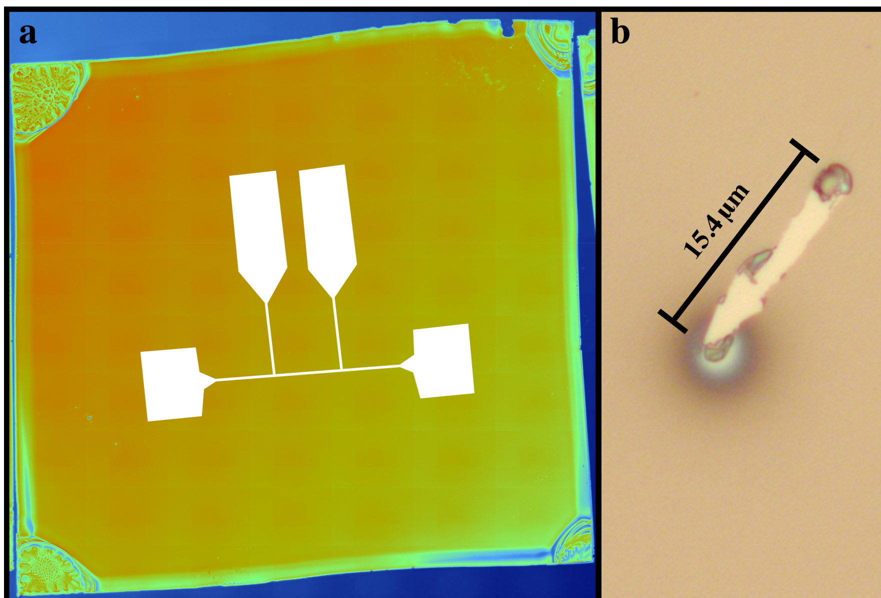

Figure P.1. **a**, image of a typical 1 cm × 1 cm sample stitched from grayscale images captured slightly out of focus using a 2.5x objective. Colors indicate arbitrary intensity from blue through green to red. 3-omega wiring structure is illustrated to scale. **b**, contamination in a ∼50 nm film after pressing on the chip surface with a soft swab. The brighter Si substrate is visible through the scratch in the PMMA film. Image was captured through a 50x objective on a yellow-light optical microscope.

contamination along the edges and especially in the corners of produced wafer chips. To evaluate the effect of different cleaning steps, a set of minimum two samples per cleaning combination of Table P.1 was imaged. From these images, it was clear that none of the additional cleaning steps after IPA had any appreciable effect. Also, it was clear that the amount of defects were more chip specific than cleaning specific, thus care was taken to always keep track of individual chips through the various process steps from this point onward.

Co-supervisor Susanne Sandell had the idea of covering the wafer surface with Scotch-tape while dicing. This led to marked reduction in contamination density in the center of the chips as readily seen by comparing Figures P.1 and P.4a. To remove any tape residues, acetone and IPA sonication was chosen as the cleaning procedure. Contamination as a result of handling is seen from the comparison of a chip and a reused 2 in wafer before and after spincoating in Figure P.3. The chips has exposed fragile Si fracture zones along all edges, while the complete wafer has no

Table P.1. Overview of investigated washing steps.

	1	2	3	4	5	6
IPA rinse	x	x	x	x	x	x
Acetone + IPA sonication			x	x	x	x
O_2 plasma clean				x		x
Hotplate at 180 °C					x	x
DI water sonication		x				

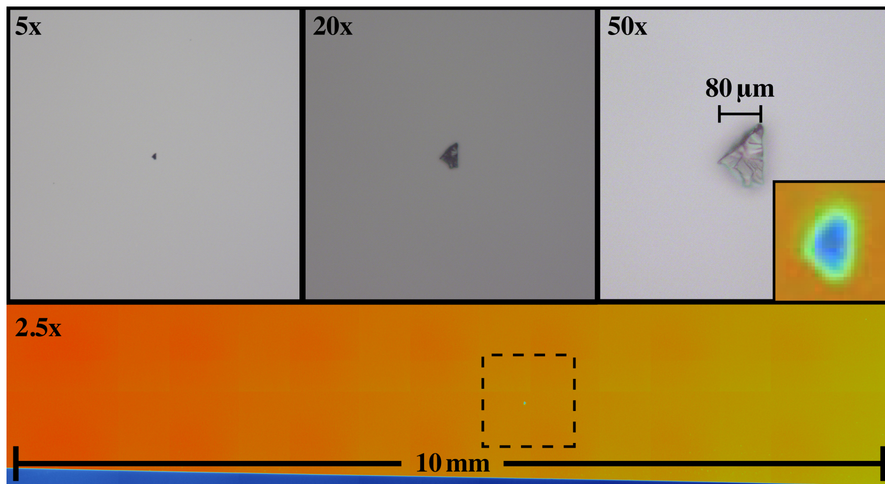

Figure P.2. Images of a contaminant particle captured at various zooms. Colors of 2.5x image indicate arbitrary grayscale intensity ranging from blue to red. Remaining images are full color, but captured under yellow light. The colored insert of the 50x image is a digitally magnification of the defect from the 2.5x image.

such sites and is only handled from one location on the edge. To minimize handling contamination, plastic tweezers were introduced and most handling was performed by grabbing the already contaminated chip corners. Additionally, polymer solution was filtered through a 0.2 µm filter as an extra precaution.

It is of high importance that there are no holes in the polymer region under the measurement structure seen in Figure P.1a, that can cause parasitic currents through the Si substrate. Visible contamination was therefore investigated by the stylus profilometer and in an optical microscope. Defects on the uncoated Si substrate appear as darker (more blue) spots. One such spot is investigated in Figure P.2 at a

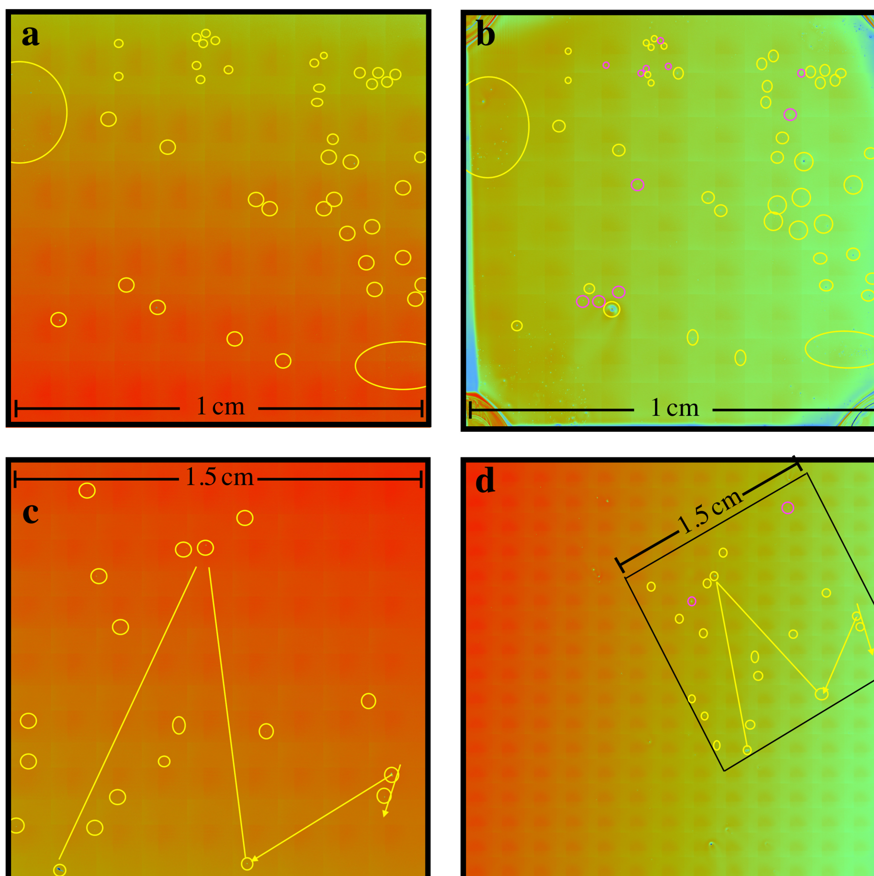

Figure P.3. **a**, **b**, contamination on a wafer chip before (**a**) and after (**b**) spincoating of a ~50 nm PMMA film. **c**, **d**, contamination on parts of a 2 in before (**c**) and after (**d**) spincoating of a ~50 nm PMMA film. Contamination present both before and after spincoating are marked in yellow and defects appearing after spincoating are marked in pink. All images are stitched from grayscale images captured slightly out of focus using a 2.5x objective. Colors indicate arbitrary intensity from blue through green to red.

range of magnifications. From its faceted appearance it is clear that it is crystalline matter, most likely Si dust from dicing. 2.5x magnification is also deemed suficient as even the shape of the particle is visible as seen from the small insert of Figure P.2. After spincoating with ~50 nm PMMA, particles have not moved, but an intensity distortion is visible in a circle around the particles, as seen in Figure P.4. Contaminant particles are orders of magnitude larger than the PMMA thickness. It was therefore believed that voids were formed around these particles, posing a significant

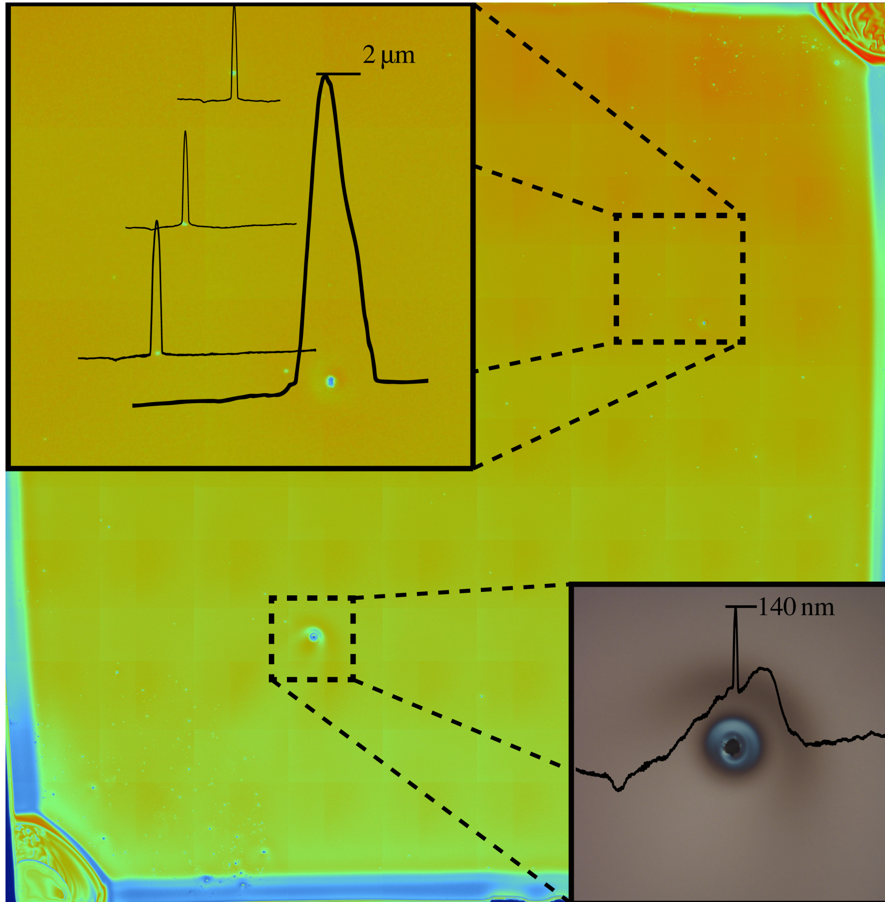

Figure P.4. A PMMA coated 1 cm × 1 cm Si chip with digital zoom (upper left) and optical zoom (lower right) of interesting film defects. Black lines of the upper left insert give defect profiles as captured by a profilometer. The four lines are drawn to scale as indicated by the 2 µm height of the largest peak. The profile of the lower left insert is also captured by profilometer, but slightly off-center with respect to the defect peak.

risk of a conductive pathway to the Si substrate. Stylus profilometer scans from Figure P.4 demonstrate, however, that no voids are observed around the defects. The unexplained negative displaced volume observed in VXI data of Chapter 4.4 of the thesis may be explained by a PMMA buildup on these contaminant particles, in line with defect type e of Figure 5.1. Presence of tall PMMA peaks are also made likely by the increased defect contrast observed after spincoating (Figure P.3b and d) and the smooth disk-shaped blue region observed in the damaged contamination site of

Figure P.1b. Both types of intensity deepening is present throughout samples and hints at high variation in polymer thickness in exactly those spots. A surface specific and material sensitive technique is, however, needed to settle this issue. For now, it is assumed that the observed defects caused by Si particles are not likely to be an issue in 3ω measurements.

In line with the new 3ω model, PMMA thicknesses 10 nm, 20 nm, 30 nm, 50 nm and 100 nm were targeted. To find suitable concentrations for this new thickness range, a calibration curve was made, starting with one new film of 1.52 wt.% and films from 1 and 5 wt.% from the thesis. Based on this curve, new solutions were made (labeled *calibration II* in Table P.2) with the aim of improving accuracy in the target range. A linear fit of thickness versus concentration yielded lower R^2 value than a power law fit in this low concentration regime. From Table P.2, it is clear that the chosen values were accurate for all produced samples, apart from the thickest film, for which concentration was overestimated by the linear fit. This sample was in any case deemed appropriate for the intended purpose. All produced films were colorless, with reflectivity decreasing as thickness increased, except for the 132 nm thick films, which were dark blue. It is clear that concentration based spin-curves more accurately predict PMMA thickness than rpm spin-curves as was also concluded in Chapter 4.1 of the thesis.

Thickness uniformity, chip-to-chip variations and changes with time are important parameters to investigate as these PMMA films will be used in highly sensitive 3ω measurements. From 7 evenly spaced points along the radian of three different samples of 20 nm, 57 nm and 132 nm thick PMMA films, no consistent change in thickness could be seen. This is in contrast to results for thicker films seen in Figure 4.5, related either to lower viscosity of low concentration films or to smaller chip size. No effect of either storing for two days or baking at 180 °C for 10 min could be found in a 57 nm thick PMMA film. Chip-to-chip variation for films from identical concentration is also below the detectable level, as seen for concentrations 0.78 wt.%, 1.52 wt.% and 1.00 wt.%. It is therefore safe to assume that PMMA thickness is identical (within the given uncertainty) for all films produced from the same concentration. The 8 % uncertainty of these measurements is higher than was measured by both AFM and the optical profiler in the thesis, and should ideally be improved to not adversely affect precision of measured TBC values. It should also be kept in mind that, although PMMA is a rather stiff polymer, it can not be ruled out that the force of the stylus tip causes a slight indentation, lowering the measured thickness. Non-invasive and accurate thickness measurement is still warranted to to

Table P.2. PMMA thickness as measured by stylus profilometry for n different lines along a step edge scratch.

Purpose	Concentration /wt.%	Mean thickness /nm	Uncertainty	n
calibration I	1.52	45.9	8.2%	11
calibration II	0.78	18.3	9.0%	9
calibration II	1.00	28.9	3.0%	5
calibration II	1.25	35.5	3.4%	4
calibration II	1.52	43.2	5.5%	3
calibration II	2.00	56.4	4.1%	4
storing for 2 days	2.00	55.1	3.0%	4
10 min at 180 °C	2.00	56.1	4.9%	7
sample	0.40	9.1	8.8%	5
sample	0.78	18.7	8.6%	5
sample	1.00	27.1	7.5%	6
sample	1.75	57.3	2.0%	5
sample	2.90	132	1.7%	8

combat these issues for all thickness ranges.

Scanning four different $(10 \times 10)\,\mu m$ areas on two samples of respectively 9 19nm with a SA-AIR cantilever in the Multimode AFM revealed no nanoscale pin-holes. The 19 nm film also appeared featureless after baking at 180 °C for 10 min, contrary to what has been observed by other authors [18, 29]. No more samples were mapped as the much thicker films of $>$500 nm from Figure 4.6 of the thesis had already proven to be smooth and largely defect-free.

Spincoated PMMA films have already proven to adhere well to Si substrates and to be resistant to scratches. It was believed, therefore that contact with soft materials such as tissue or padded swabs would not cause any harm. Tests, however, revealed that lateral movement during contact with a soft swab caused previously noted PMMA-covered Si particles to be dragged along the surface, creating gashes in the PMMA film as seen in Figure P.1b. Surface contact was not avoided during packing of 3ω samples produced during the thesis work, possibly explaining the observed short-circuiting. Now, care was taken to firmly attach all chips by tape, only pressing on the corners of the chips. Additionally, five chips of each thickness were produced for redundancy. If PMMA defect issues prove to be a persistent problem

also with this sample set, omitting dicing and shipping is suggested as the two most crucial improvements. Dicing was necessary herein, due to size restrictions in the 3ω setup, but sufficiently small wafers or the use of a dicing saw may improve the issue. Depositing the 3ω Au measurement structure seen in Figure P.1a should be performed in Norway to significantly lower the risk of contamination and defect formation during shipping.

Conclusion

Si-SiO_x-PMMA samples with five different film thicknesses were fabricated and shipped to Spain for 3ω measurements. Extreme care was taken to develop a protocol for producing defect-free PMMA films, especially minimizing adverse effects of Si particle contamination from dicing. The developed protocol is believed to be a both repeatable and fast method for producing large amounts of PMMA covered chips with very few defects located in the center of the samples.